



HAL
open science

On the stability of POD Basis Interpolation via Grassmann Manifolds for Parametric Model Order Reduction in Hyperelasticity

Orestis Friderikos, Emmanuel Baranger, Marc Olive, David Néron

► **To cite this version:**

Orestis Friderikos, Emmanuel Baranger, Marc Olive, David Néron. On the stability of POD Basis Interpolation via Grassmann Manifolds for Parametric Model Order Reduction in Hyperelasticity. 2020. hal-02902214v1

HAL Id: hal-02902214

<https://hal.science/hal-02902214v1>

Preprint submitted on 18 Jul 2020 (v1), last revised 24 Oct 2022 (v3)

HAL is a multi-disciplinary open access archive for the deposit and dissemination of scientific research documents, whether they are published or not. The documents may come from teaching and research institutions in France or abroad, or from public or private research centers.

L'archive ouverte pluridisciplinaire **HAL**, est destinée au dépôt et à la diffusion de documents scientifiques de niveau recherche, publiés ou non, émanant des établissements d'enseignement et de recherche français ou étrangers, des laboratoires publics ou privés.

On the stability of POD Basis Interpolation via Grassmann Manifolds for Parametric Model Order Reduction in Hyperelasticity

Orestis Friderikos*, Emmanuel Baranger, Marc Olive*, David Néron

Université Paris-Saclay, ENS Paris-Saclay, CNRS, LMT - Laboratoire de Mécanique et Technologie, 94235, Cachan, France.

Abstract

A rigorous mathematical approach on the Proper Orthogonal Decomposition (POD) basis interpolation via Grassmann manifolds for parametric Model Order Reduction (pMOR) is given. The work focuses on issues related to interpolation on Grassmann manifolds making a concrete elucidation of the local character of linearization. It is shown how the stability of the interpolation can be lost if certain geometrical conditions are met. To this effect, we draw special attention to the injectivity radius and the cut-locus on the Grassmannian which are essential to establish well defined local maps. Here, pMOR is applied in hyperelastic structures using a non-intrusive approach for inserting the interpolated spatial POD ROM basis in a commercial code. The accuracy of the method is assessed by a posteriori error norms defined using the ROM FEM solution and its high fidelity counterpart simulation. High quality correlations of the error norms are found for both numerical examples. One important outcome concerns the accuracy with respect to the number of POD modes in which the error norm shows a non-monotonic decrease with a spurious oscillatory behavior.

Keywords: Parametric Model Order Reduction (pMOR), Proper Orthogonal Decomposition, Grassmann manifolds, Hyperelasticity

*Corresponding author.

Email addresses: friderikos@lmt.ens-cachan.fr (Orestis Friderikos),
emmanuel.baranger@ens-paris-saclay.fr (Emmanuel Baranger),
marc.olive@math.cnrs.fr (Marc Olive), david.neron@ens-cachan.fr (David Néron)

Contents

1	Introduction	3
2	Problem Formulation	7
3	Proper Orthogonal Decomposition and Grassmannian manifold	7
4	Notions and Results about Grassmann Manifolds	9
4.1	The Grassmann Manifold and its Riemannian metric	10
4.2	Geodesic distance and principal Jordan angles	12
4.3	Exponential and logarithmic map	13
5	ROM Adaptation Based on Interpolation in Grassmann Manifolds	16
5.1	Lagrange Interpolation	17
6	Application to Hyperelasticity	18
6.1	Kinematics of Continuum Mechanics Framework	18
6.2	Incompressible Transverse Isotropic Material	19
6.3	Linearization of the principle of internal virtual work in the spatial description	19
7	Numerical Investigations	20
7.1	Abaqus implementation of POD-ROM approximations	20
7.2	Inflation of a spherical balloon	21
7.3	Hyperelastic structure with multiple components	30
8	Conclusions	35
9	Acknowledgements	35
Appendix A	Derivation of the Green-Naghdi objective rate	35
Appendix B	Grassmannian distances and injectivity radius	37

1. Introduction

Computational modeling of hyperelastic structures have been progressively used for surgical and diagnostic procedures to guide clinical studies. In these numerical problems, challenges often arise due to large scale models, complexity, geometric non-linearity, advanced constitutive equations and contact. All these difficulties lead to severe stability/convergence issues in FEM codes accompanied with high computational times. Therefore, solutions are in general obtained on High Performance Computing (HPC) clusters with process time which can take hours, days, or even weeks [49]. Due to large demands on computational resources, some studies, for instance the need of representing variations of material parameter values are out of the reach of today’s facilities.

In the meanwhile, Reduced-Order Models (ROM) aim to decrease the computational burden of large-scale systems and solve parametrized problems by generating models with lower complexity, but accurately enough to represent the high fidelity counterpart simulations. One popular method is the Proper Orthogonal Decomposition (POD) [36, 27, 48], also known as Kharhunen-Loève Decomposition (KLD) [3, 9], Singular Value Decomposition (SVD) [17] or Principal Component Analysis (PCA) [26, 33]. We need to emphasize that all these POD techniques are referred as *a posteriori* as they require some knowledge (at least partial) on the solution of the problem.

Parametric Model Order Reduction (pMOR) is used to generate a ROM model that approximates a full-order system with high accuracy over a range of parameters. In case of solving a parametric problem using the POD, the method starts by a sampling stage during which the full-order system is solved for some rather small set of *training* parameters. The state variable field ‘*snapshots*’ are then compressed using the POD method to generate a ROM basis that is expected to reproduce the most characteristic dynamics of its high-fidelity counterpart. Nevertheless, since the POD bases are generated for a set of training points, they are optimal only to these parameters. Thus, a main drawback of POD is the sensitivity to parameter changes and the lack of robustness over the entire parameter space. Consequently, any ROM basis generated by the approach outlined above cannot be expected to give a good approximation away from the training point. In pMOR, the question we have to address is how to compute a good approximation of the POD basis related to a *new parameter*. Multiple methods have been proposed for adapting POD basis to address parameter variation as thoroughly documented in related

review articles [42, 50, 41].

For nonlinear systems, even though a Galerkin projection reduces the number of unknowns, the computational burden for obtaining the solution could still be high due to the prohibitive computational costs involved in the evaluation of nonlinear terms. Hence, the nonlinear Galerkin projection in principle leads to a ROM but its evaluation could be more expensive than the evaluation of the original problem. To this effect, to make the resulting ROMs computationally efficient, POD is typically used together with a sparse sampling method, also called *hyper reduction*, such as the missing point estimation (MPE) [31], the empirical interpolation method (EIM) [43], the discrete empirical interpolation method (DEIM) [34], the Gappy POD method [16], and the Gauss-Newton with approximated tensors (GNAT) method [38].

Parametric Model Order Reduction using POD has been scarcely applied in hyperelasticity. Here, pMOR is used to hyperelastic structures by adapting pre-computed POD basis on Grassmann manifolds. We import what is done initially in the field of computational fluid dynamics which was proposed for parametrized systems that are linear in state [51, 32, 46, 48]. It is also worthy to mention the work in [37] on real time simulations of hyperelastic structures using POD basis interpolation on Grassmann manifolds in combination with an asymptotic numerical method. The contribution here targets on the part of pMOR related to the interpolation procedure focused on certain geometrical conditions under which the numerical stability is preserved.

When addressing the question of *POD basis interpolation*, the main point is that *interpolation cannot be done in a linear space*. Indeed, any POD basis can be performed by some matrix $\mathbf{M} \in \text{Mat}_{n,p}(\mathbb{R})$, which is not uniquely defined. Now, despite the appearances, computation can not be done in the linear space $\text{Mat}_{n,p}(\mathbb{R})$ of matrices, but in a *quotient space*, meaning that the result has to be independent of the *choice* of such matrix \mathbf{M} . In mathematics, this idea to make computation independently of some choice leads to the notion of a *manifold* [10]. In the specific case of POD basis, the involved manifold is the classical *Grassmann manifold*, defined as the set of fixed dimensional sub-spaces of some \mathbb{R}^n . Such Grassmann manifold interpolation is well documented [32, 46, 48, 22, 28], all coming from the fluid mechanics community, and computation can be done explicitly.

Thus, we might have been satisfied with a simple application of the existing and now well-known formulas. However, applying formulae in manifolds

requires the verification of certain conditions. Indeed, these formulae are in fact used to perform a linearization, which is a generalization of what is done on a $2D$ sphere: locally, one can identify a plane to a sphere. Now, the formulae are obtained from certain applications, called here logarithm (to linearize) and exponential (to return to the curved space). Such applications are defined only locally, and the calculations can only be stable if this local condition is verified. To our knowledge, this crucial point seems to have been clarified only in the recent work of Mosquera et al. [46, 48] who recall a theoretical result on the *injectivity radius* of the exponential function. Indeed, in our case which is a specific example of a Riemannian manifold [13], it is always possible to construct a disk inside which the logarithmic and exponential functions are inverse to each other, and thus the linearization process is guaranteed to be totally stable in this disk. It would therefore seem necessary, for any preamble, to verify that the interpolation only takes place on the condition of being inside such a disk. What we noticed then, is that the formulae can apply even outside this disk, which we did, but we stress here that under such conditions, calculations have no reason to be relevant. We then make a conjecture which is purely mathematical: it is not so much the notion of the injectivity radius that is involved here as the notion of *cut-locus* [13], which remains to be further developed and specified in the case of Grassmann manifold. Up to our knowledge, such a notion was very quickly overlooked by [4], who states a result without any proof. Therefore, to be able to specify and clarify all these theoretical questions we have decided to take up the essential mathematical points concerning Grassmannian manifolds. Thus, we insist on the local character of these formulae and the necessary mathematical rigour that this implies in their handling. To emphasize all such theoretical difficulties, we propose the simple example of an interpolation on a $2D$ cylinder, where injectivity radius and cut-locus can be exhibited.

Another unexpected observation is that the numerical studies conducted here revealed a spurious oscillatory behavior of the error norm, i.e., random non-monotone decreasing error patterns with respect to the number of POD modes. And this outcome provided even by the rather trivial hyperelastic structures chosen in this study. The interesting thing about this fact is that it does not seem special to the hyperelasticity problems. Thus, a relevant behavior might exist in other engineering fields, as for example in benchmark problems emerging from the CFD analysis (aeroelasticity, laminar or turbulent wakes behind a circular cylinder, etc).

Finally, whether for the problems of injectivity radius, of cut-locus or non-monotone decreasing error, it therefore seemed essential to us to detail a theoretical mathematical part that allows us to set clear definitions and constraints.

Considering the *mechanical part*, the overall procedure comprises an off-line and an on-line stage. The off-line stage characterizes the potentially costly procedure of solving FEM problems associated with different values of the physical or modeling parameter (training points). The on-line stage consists of POD basis interpolation on Grassmann manifolds to determine a ROM basis for an unseen target parameter. Then, a non-intrusive approach is introduced for the obtained spatial POD basis. Note, that this approach deviates from the POD methods that relying on a Galerkin/Petrov Galerkin projection on the governing equations. Instead, ROM-FEM models are implemented by inserting the interpolated spatial POD basis using linear constraint equations in Abaqus. It is evident that, by constraining the degrees of freedom, the reduced model still embeds the high dimension. We remark that we followed this approach using a commercial code only for evaluating the accuracy of the adaption of POD basis via interpolation on Grassmann manifolds. It is not our objective to implement a method of nonlinear model reduction for the effective evaluation of the nonlinear terms, although it is a quite challenging task to be realized inside a commercial code.

For the pMOR, two hyperelastic structures modeled with isotropic and anisotropic constitutive laws are studied. Specifically, for the anisotropic model, a subclass of transversely isotropic materials is considered. In this subclass, the strain energy function is assumed to depend only on two invariant measures of finite deformation [30, 21, 20, 24]. At the numerical examples, the decision made here is to enter the parameters in two ways considering a) the model anisotropy defined by the fiber orientation, and b) the material coefficients of the hyperelastic constitutive equations.

The present paper is organized as follows. From [section 3](#) to [section 5](#) we only focus on the *theoretical background*, so we produce definitions and theorems in a mathematical way. Once again, we emphasize here that all this is done to clarify the rigor required to perform the calculations. More specifically, the Proper Orthogonal Decomposition and the orthonormal basis representation of subspaces on Grassmann manifolds are discussed in [section 3](#). Then [section 4](#), introduces some basic notions and results about the geometry of Grassmann manifolds whereas [section 5](#) provides the computational framework for the reduced order model adaptation based on interpolation

on Grassmann manifolds. The mechanical part starts with [section 6](#), which covers the framework of hyperelasticity theory in continuum mechanics for an incompressible transverse isotropic material. In [section 7](#), the interpolation performance using two hyperelastic structures is shown, and further important computational aspects are discussed. Finally, [section 8](#) highlights the main results and some important outcomes.

2. Problem Formulation

We consider some mechanical problem governed by a specific parameter $\lambda \in [\lambda_{min}, \lambda_{max}] \subset \mathbb{R}$, which comes from hyperelasticity in our situation (see [section 6](#)). For each parameter λ , the solution is given by a space-time smooth field

$$(t, \mathbf{X}) \in [0; T] \times \Omega_0 \mapsto u^\lambda(\mathbf{X}, t) \in \mathbb{R}^3$$

where Ω_0 is a closed convex subset of \mathbb{R}^3 and $T > 0$.

To avoid costly computations for all values $\lambda \in [\lambda_{min}, \lambda_{max}]$, we would like to interpolate between a finite number of FEM solutions $u_i := u^{\lambda_i}$, associated to N training points $\lambda_1, \dots, \lambda_N$. In fact, it is at the level of the POD performed on the snapshot matrices $\mathbf{S}(\lambda_i)$ (defined in the next section) associated to the solutions u_i that this interpolation will be considered. But one of the essential points of this POD is that it associates to each snapshot matrix $\mathbf{S}(\lambda_i)$ a certain point \mathbf{m}_i of a Grassmannian manifold \mathcal{G} , and it is therefore needed at this stage to interpolate between points $\mathbf{m}_1, \dots, \mathbf{m}_N$ on \mathcal{G} . It is now proposed to detail the link between a POD reduction and the construction of a point on a Grassmannian manifold.

3. Proper Orthogonal Decomposition and Grassmannian manifold

The POD method can be applied to curves defined in Hilbert spaces of infinite dimension. The initial idea is to determine a subspace of a given dimension p (which is the fixed number of modes of the POD), allowing to reflect “as well as possible” this curve, as it is very well explained in [\[27, 46\]](#). In most cases, however, we do not consider the entire curve, but only a finite number of points of a Hilbert space $\mathcal{H}_{\text{spatial}} = \mathbb{R}^{N_s}$ of finite dimension N_s (the number of space points). More precisely any FEM solution u of our problem under consideration produces a *snapshot matrix*

$$\mathbf{S}_{jk}, \quad 1 \leq j \leq 3N_s, \quad 1 \leq k \leq N_t$$

with N_t the number of time steps. Such matrix encodes in fact N_t vectors $\mathbf{u}_k := u(\cdot, t_k) \in \mathcal{H}_{\text{spatial}}$, and we write

$$\mathbf{S} := [\mathbf{u}_1, \dots, \mathbf{u}_{N_t}]$$

Take now $\langle \cdot, \cdot \rangle$ to be the standard inner product of the Hilbert space $\mathcal{H}_{\text{spatial}}$. To any p dimensional vector subspace \mathcal{V}_p of $\mathcal{H}_{\text{spatial}}$, there is an associated orthogonal projection

$$\pi_p : \mathcal{H}_{\text{spatial}} \longrightarrow \mathcal{V}_p$$

and the POD method address the question to minimize the distance function

$$\mathcal{J}(\mathcal{V}_p) := \sum_{k=1}^{N_t} \|\mathbf{u}_k - \pi_p(\mathbf{u}_k)\|^2, \quad \|\cdot\| := \sqrt{\langle \cdot, \cdot \rangle}$$

over all p dimensional subspaces \mathcal{V}_p . It then appears that the set of all such subspaces define a *smooth compact Riemannian manifold* [10, 13]

$$\mathcal{G}(p, n) := \{\mathcal{V}_p \subset \mathcal{H}_{\text{spatial}}, \quad \dim(\mathcal{V}_p) = p\}, \quad n := 3N_s$$

so that any p dimensional vector subspace \mathcal{V}_p can be considered as some *point* $\mathbf{m} \in \mathcal{G}(p, n)$, and the question is finally to minimize $\mathcal{J}(\mathbf{m})$ over all $\mathbf{m} \in \mathcal{G}(p, n)$.

In practice, let consider an orthonormal basis ϕ_1, \dots, ϕ_p of \mathcal{V}_p so that the matrix form of π_p is given by

$$\Phi_p \Phi_p^T, \quad \Phi_p := [\phi_1, \dots, \phi_p] \in \text{Mat}_{n,p}(\mathbb{R})$$

where $\text{Mat}_{n,p}(\mathbb{R})$ is the vector space of $n \times p$ matrices, and (right) superscript $(\cdot)^T$ denotes the transposition operation. By direct computation, the distance function \mathcal{J} is then rewritten

$$\mathcal{J}(\mathbf{m}) = \|\mathbf{S} - \Phi_p \Phi_p^T \mathbf{S}\|_{\text{F}}^2$$

where $\|\mathbf{A}\|_{\text{F}} := \sqrt{\text{tr}(\mathbf{A}\mathbf{A}^T)}$ is the Frobenius norm on $\text{Mat}_{n,p}(\mathbb{R})$.

Now it is classically known that minimization of \mathcal{J} is given by Eckart–Young Theorem [2, 11, 17, 7] and can be obtained via a *singular value decomposition* of \mathbf{S} . Indeed, take this SVD to be

$$\mathbf{S} = \mathbf{U}\mathbf{\Sigma}\mathbf{V}^T, \quad \mathbf{U} := [\phi_1, \dots, \phi_{N_t}]$$

with singular values $\sigma_1 \geq \sigma_2 \geq \dots \geq \sigma_{N_t}$. Then one solution of minimizing \mathcal{J} is given by

$$\mathbf{m}_0 := \text{span}(\phi_1, \dots, \phi_p)$$

which is unique whenever $\sigma_p > \sigma_{p+1}$ [27]. Let also define the *reduced model* \mathbf{S}_p of our snapshot matrix by

$$\mathbf{S}_p := \mathbf{\Phi}_p \mathbf{\Phi}_p^T \mathbf{S}, \quad \mathbf{\Phi}_p := [\phi_1, \dots, \phi_p].$$

Taking back our snapshot matrices $\mathbf{S}(\lambda_i)$ associated to operating points λ_i , we thus obtain for any fix mode $p \geq 1$ points

$$\mathbf{m}_i := \text{span}(\phi_1^{(i)}, \dots, \phi_p^{(i)}) \in \mathcal{G}(p, n), \quad i = 1, \dots, N.$$

Let now explain in more detail the geometry of such a manifold so that we can interpolate between these points.

4. Notions and Results about Grassmann Manifolds

Let now be given some points defined on a compact smooth Riemannian manifold, which only look *locally* like an euclidean vector space. From the general theory of manifolds, such sets can be described using *local charts* and a pointwise metric [39, 10, 13]. Compare to the simple case of an *open subset* of some vector space, one may need several charts to describe all the manifold.

It should be recalled that the specific case of the Grassmannian manifolds has been particularly studied in the context of POD interpolation methods [28, 32, 22, 46, 48, 47], and we give again here the main ideas of these articles. It should also be noted that a very mathematical (and very systematic) approach to these manifolds is proposed by Kozlov [19].

A Grassmannian manifold $\mathcal{G}(p, n)$ can be obtained as a *quotient space* [39, Chapter 21] of the (open) space of p linearly independent vectors of \mathbb{R}^n . More specifically [35, Appendix C.2], first define the (non-compact) Stiefel manifold $\mathcal{S}^{nc}(p, n)$ to be the set of p linearly independent vectors $\{\mathbf{y}_1, \dots, \mathbf{y}_p\}$ of \mathbb{R}^n . Taking any basis of \mathbb{R}^n , such a set can be represented by a rank p matrix

$$\mathbf{Y} := [\mathbf{y}_1, \dots, \mathbf{y}_p] \in \text{Mat}_{n,p}(\mathbb{R}).$$

This lead to define a *fiber bundle* [18, 15], which is also a *submersion* [39]:

$$\pi : \mathbf{Y} \in \mathcal{S}^{nc}(p, n) \mapsto \pi(\mathbf{Y}) = \mathbf{m} := \{\mathbf{Y}\gamma, \quad \gamma \in \text{GL}(p)\} \in \mathcal{G}(p, n) \quad (1)$$

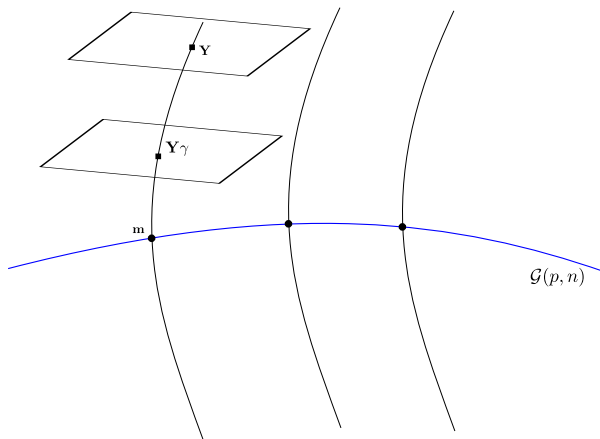


Figure 1: Schematic of a fiber bundle.

Informally speaking, it means that any point \mathbf{m} of the Grassmannian manifold $\mathcal{G}(p, n)$ can be represented by any point \mathbf{Y} of the *fiber* $\pi^{-1}(\mathbf{m})$ (Figure 1).

From this submersion, the Grassmannian manifold $\mathcal{G}(p, n)$ can inherit the geometry of the Stiefel manifold $\mathcal{S}t^{nc}(p, n)$. As this last manifold is in fact an *open space* of the vector space $\text{Mat}_{n,p}(\mathbb{R})$, we have only one chart, so that it has a “simple” geometry.

Remark 4.1. Some also consider a submersion using the *compact Stiefel manifold*

$$\mathcal{S}t^c(p, n) := \{\bar{\mathbf{Y}} \in \text{Mat}_{n,p}(\mathbb{R}), \quad \bar{\mathbf{Y}}^T \bar{\mathbf{Y}} = \mathbf{I}_p\}$$

where $\mathbf{I}_p \in \text{Mat}_{n,p}(\mathbb{R})$ is the identity matrix, so that we have

$$\pi^c : \bar{\mathbf{Y}} \in \mathcal{S}t^c(p, n) \mapsto \pi^c(\bar{\mathbf{Y}}) = \mathbf{m} := \{\bar{\mathbf{Y}}g, \quad g \in \text{O}(p)\} \in \mathcal{G}(p, n)$$

4.1. The Grassmann Manifold and its Riemannian metric

So far, we have only described the *points* of the manifold $\mathcal{G}(p, n)$. Let now explain its Riemannian structure [13]. To do so, first attach to each $\mathbf{m} \in \mathcal{G}(p, n)$ a *tangent space*, which is a vector space isomorphic to $\mathbb{R}^{p \times (n-p)}$, equipped with a scalar product (depending smoothly on \mathbf{m}), so that $\mathcal{G}(p, n)$ becomes a Riemannian manifold.

First of all, as $\mathcal{S}t^{nc}(p, n)$ is an open space of $\text{Mat}_{n,p}(\mathbb{R})$, the tangent space attached to any $\mathbf{Y} \in \mathcal{S}t^{nc}(p, n)$ is simply given by $\text{Mat}_{n,p}(\mathbb{R})$, and a natural inner product of $\text{Mat}_{n,p}(\mathbb{R})$ is given by

$$\langle \mathbf{A}, \mathbf{B} \rangle := \text{tr}(\mathbf{A}^T \mathbf{B}).$$

But we need to define on each point $\mathbf{Y} \in \mathcal{S}t^{nc}(p, n)$ a scalar product $\langle \cdot, \cdot \rangle_{\mathbf{Y}}$ which is right $\text{GL}(p)$ invariant (so that this scalar product can be transferred to the point $\mathbf{m} = \pi(\mathbf{Y})$), meaning that

$$\langle \mathbf{A}\gamma, \mathbf{B}\gamma \rangle_{\mathbf{Y}\gamma} = \langle \mathbf{A}, \mathbf{B} \rangle_{\mathbf{Y}}.$$

One candidate is given by [4, 28]:

$$\langle \mathbf{A}, \mathbf{B} \rangle_{\mathbf{Y}} := \text{tr}((\mathbf{Y}^T \mathbf{Y})^{-1} \mathbf{A}^T \mathbf{B}).$$

Using submersion π given by (1), such a metric is transferred to any tangent vector

$$v \in T_{\mathbf{m}}\mathcal{G}(p, n), \quad \pi(\mathbf{Y}) = \mathbf{m}.$$

Nevertheless, there is no any intrinsic way to describe the tangent space $T_{\mathbf{m}}\mathcal{G}(p, n)$. Indeed, it depends on a choice of a point $\mathbf{Y} \in \pi^{-1}(\mathbf{m})$, so the *horizontal space* is defined by:

$$\text{Hor}_{\mathbf{Y}} := \{\mathbf{Z} \in \text{Mat}_{n,p}(\mathbb{R}), \quad \mathbf{Z}^T \mathbf{Y} = \mathbf{0}\}.$$

Finally

1. The tangent space $T_{\mathbf{m}}\mathcal{G}(p, n)$ is isomorphic to any $\text{Hor}_{\mathbf{Y}}$ with \mathbf{Y} such that $\pi(\mathbf{Y}) = \mathbf{m}$. An isomorphism is given by

$$d\pi_{\mathbf{Y}|_{\text{Hor}_{\mathbf{Y}}}} : \text{Hor}_{\mathbf{Y}} \longmapsto T_{\mathbf{m}}\mathcal{G}(p, n)$$

2. For any $v \in T_{\mathbf{m}}\mathcal{G}(p, n)$, the unique $\mathbf{Z} \in \text{Hor}_{\mathbf{Y}}$ such that

$$d\pi_{\mathbf{Y}} \cdot \mathbf{Z} = v \tag{2}$$

is called an *horizontal lift* of v .

3. For any $\gamma \in \text{GL}(p)$, then $\mathbf{Z}\gamma$ is another horizontal lift of v (but belonging to the vector space $\text{Hor}_{\mathbf{Y}\gamma}$) and

$$d\pi_{\mathbf{Y}\gamma} \cdot (\mathbf{Z}\gamma) = v.$$

The Riemannian metric on the Grassmannian $\mathcal{G}(p, n)$ is then defined by

$$\langle v_1, v_2 \rangle_{\mathbf{m}} := \langle \mathbf{Z}_1, \mathbf{Z}_2 \rangle_{\mathbf{Y}},$$

with $\pi(\mathbf{Y}) = \mathbf{m}$ and \mathbf{Z}_1 (resp. \mathbf{Z}_2) a horizontal lift of v_1 (resp. v_2) in $\text{Hor}_{\mathbf{Y}}$.

4.2. Geodesic distance and principal Jordan angles

The Grassmannian manifold $\mathcal{G}(p, n)$ being equipped with a Riemannian metric, we can define its associated *Levi-Civita connection* [13, 39], and then the *geodesics* associated to this connection [18, p. III.6].

We can also address the question of *minimizing curves* in $\mathcal{G}(p, n)$. To do so, let first define the *length* of any curve $c : [0; 1] \rightarrow \mathcal{G}(p, n)$ to be

$$L(c) = \int_0^1 \langle \dot{c}(t), \dot{c}(t) \rangle_{c(t)} dt$$

and define the associated *Riemannian distance*

$$d_r(\mathbf{m}_0, \mathbf{m}_1) := \inf\{L(c), \quad c(0) = \mathbf{m}_0, c(1) = \mathbf{m}_1\}. \quad (3)$$

A minimizing curve is finally some curve which realize the Riemannian distance between two points (as we are in case of a connected manifold [44]). In the general case, such minimizing curve may not exist. Nevertheless in our situation:

1. All minimizing curves are geodesics [44, Theorem 6.4];
2. Geodesics are minimizing curves only *locally* [44, Proposition 6.11].

Returning back to the Riemannian manifold $\mathcal{G}(p, n)$, there is a way to obtain explicit geodesics [19, 28]:

Theorem 4.2. *Let $\mathbf{m} \in \mathcal{G}(p, n)$ and $v \in T_{\mathbf{m}}\mathcal{G}(p, n)$ with horizontal lift given by $\mathbf{Z} \in \text{Hor}_{\mathbf{Y}}$, $\pi(\mathbf{Y}) = \mathbf{m}$. Let $\mathbf{Z} = \mathbf{U}\Sigma\mathbf{V}^T$ be a singular value decomposition of \mathbf{Z} . Then*

$$\alpha_v : t \in \mathbb{R} \mapsto \pi \left(\mathbf{Y}(\mathbf{Y}^T\mathbf{Y})^{-1}\mathbf{V} \cos(t\Sigma) + \mathbf{U} \sin(t\Sigma) \right) \in \mathcal{G}(p, n) \quad (4)$$

is the unique maximal geodesic such that $\alpha_v(0) = \mathbf{m}$ and $\dot{\alpha}_v(0) = v$.

To obtain the Riemannian distance between any two points \mathbf{m}_0 and \mathbf{m}_1 of $\mathcal{G}(p, n)$, there is now an important result [4, 19] that links this distance to the Jordan principal angles [1, 6]:

Definition 4.3. Let \mathbf{m}_0 and \mathbf{m}_1 be two points in $\mathcal{G}(p, n)$ and define $\overline{\mathbf{Y}}_i \in \pi^{-1}(\mathbf{m}_i)$ ($i = 0, 1$) such that $\overline{\mathbf{Y}}_i^T \overline{\mathbf{Y}}_i = \mathbf{I}_p$. Writing a singular value decomposition

$$\overline{\mathbf{Y}}_0^T \overline{\mathbf{Y}}_1 = \mathbf{U}\Sigma\mathbf{V}, \quad \Sigma = \text{diag}(\sigma_1, \dots, \sigma_p), \quad 0 \leq \sigma_p \leq \dots \leq \sigma_1 \leq 1$$

then the Jordan principal angles between \mathbf{m}_0 and \mathbf{m}_1 are given by

$$0 \leq \theta_i := \arccos \sigma_i \leq \frac{\pi}{2}$$

As a consequence of [19, Theorem 12.2], for any two points \mathbf{m}_0 and \mathbf{m}_1 of $\mathcal{G}(p, n)$ the Riemannian distance is given by

$$d_r(\mathbf{m}_0, \mathbf{m}_1) = \left(\sum_{i=1}^p \theta_i^2 \right)^{1/2} \quad (5)$$

and the *diameter* of $\mathcal{G}(p, n)$ (the maximum distance between two points) is given by [19]

$$\text{diam} = \sqrt{r} \frac{\pi}{2}, \quad r = \min(p, n - p) \quad (6)$$

Remark 4.4. From Hopf-Rinow Theorem [13, Theorem 2.103], any two points of the Grassmannian manifold can be joined by a minimal geodesic. If we explicitly find such a geodesic among all the ones given by (4), we can deduce the distance, but this is far from being obvious. Formula (5) not allows us to find explicit geodesic.

4.3. Exponential and logarithmic map

By exploiting geodesics of a Riemannian manifold, it is possible to establish local maps (using *normal coordinates* [13]), in particular through the exponential function. In the case of the (complete) Grassmannian manifold $\mathcal{G}(p, n)$, such an exponential map makes it possible to obtain, at any point $\mathbf{m} \in \mathcal{G}(p, n)$, an application between the tangent space $T_{\mathbf{m}}\mathcal{G}(p, n)$ and an open subset of $\mathcal{G}(p, n)$.

Let now recall definition of the exponential map [44]:

Definition 4.5. Let $\mathbf{m} \in \mathcal{G}(p, n)$, then the exponential map at \mathbf{m} is defined by

$$\text{Exp}_{\mathbf{m}} : T_{\mathbf{m}}\mathcal{G}(p, n) \longrightarrow \mathcal{G}(p, n), \quad v \mapsto \text{Exp}_{\mathbf{m}}(v) := \alpha_v(1)$$

where α_v is given by (4).

From this exponential map, it is thus possible to simply write down any geodesic with initial velocity v :

$$t \in \mathbb{R} \mapsto \text{Exp}_{\mathbf{m}}(tv). \quad (7)$$

However, there is no reason why this geodesic should be a minimizing one between $\mathbf{m} = \text{Exp}_{\mathbf{m}}(0)$ and $\mathbf{m}_1 := \text{Exp}_{\mathbf{m}}(t_1v)$ for any $t_1 > 0$.

Remark 4.6. The length of the geodesic (7) between the points $\mathbf{m} = \text{Exp}_{\mathbf{m}}(0)$ and $\mathbf{m}_1 = \text{Exp}_{\mathbf{m}}(t_1 v)$ is simply given by $t_1 \|v\|$. Taking a horizontal lift \mathbf{Z} of v , we thus obtain the length

$$t_1 \|v\| = t_1 \|\mathbf{Z}\|_F$$

which is not, in general, the Riemannian distance $d_r(\mathbf{m}_0, \mathbf{m}_1)$ given by (3).

There is no reason now that the exponential map can be injective:

Definition 4.7. For any point $\mathbf{m} \in \mathcal{G}(p, n)$, the *injectivity radius* at \mathbf{m} is defined to be

$r_{\mathbf{m}} := \sup\{r > 0, \quad \text{Exp}_{\mathbf{m}} : \text{B}(0, r) \longrightarrow \text{Exp}_{\mathbf{m}}(\text{B}(0, r)) \text{ is a diffeomorphism}\}$
 where $\text{B}(0, r) := \{v \in T_{\mathbf{m}}\mathcal{G}(p, n), \quad \|v\| < r\}$. The injectivity radius r_g of $\mathcal{G}(p, n)$ is given by

$$r_g := \inf\{r_{\mathbf{m}}, \quad \mathbf{m} \in \mathcal{G}(p, n)\}.$$

Such an injectivity radius r_g just make sure that, for any point $\mathbf{m} \in \mathcal{G}(p, n)$, the map $\text{Exp}_{\mathbf{m}}$ is a diffeomorphism from $\text{B}(0, r_g)$ onto its image. Of course, it may happen that $\text{Exp}_{\mathbf{m}}$ is a diffeomorphism on some bigger open set $U \supset \text{B}(0, r_g)$, so we can consider its inverse map on $\text{Exp}_{\mathbf{m}}(U)$.

Now, in the specific case of Grassmannian manifold, we have:

Theorem 4.8 ([19]). *For any integers n, p such that $\min(p, n - p) \geq 2$, the injectivity radius of $\mathcal{G}(p, n)$ is given by*

$$r_g = \frac{\pi}{2}$$

As there is an explicit formulae for the geodesics, and thus for the exponential map, it is also possible to define an explicit *logarithm map*. First define for any point $\mathbf{m} \in \mathcal{G}(p, n)$ the open set

$$U_{\mathbf{m}} := \{\mathbf{m}_1 \in \mathcal{G}(p, n), \quad \mathbf{Y}^T \mathbf{Y}_1 \text{ is invertible}, \quad \pi(\mathbf{Y}) = \mathbf{m}, \quad \pi(\mathbf{Y}_1) = \mathbf{m}_1\} \quad (8)$$

Definition 4.9 (Logarithm map in Grassmannian manifold). For any $\mathbf{m} \in \mathcal{G}(p, n)$, the logarithm map at \mathbf{m} is defined on the open space $U_{\mathbf{m}}$ given as above by

$$\mathbf{m}_1 \in U_{\mathbf{m}} \mapsto \text{Log}_{\mathbf{m}}(\mathbf{m}_1) = d\pi_{\mathbf{Y}} \cdot (\mathbf{U} \arctan(\boldsymbol{\Sigma}) \mathbf{V}^T) \in T_{\mathbf{m}}\mathcal{G}(p, n) \quad (9)$$

where $\pi(\mathbf{Y}_1) = \mathbf{m}_1$, $\pi(\mathbf{Y}) = \mathbf{m}$ and

$$\left[\mathbf{Y}_1 (\mathbf{Y}^T \mathbf{Y}_1)^{-1} (\mathbf{Y}^T \mathbf{Y}) - \mathbf{Y} \right] (\mathbf{Y}^T \mathbf{Y})^{-1/2} = \mathbf{U} \boldsymbol{\Sigma} \mathbf{V}^T$$

In fact we now have:

Lemma 4.10. *For any $\mathbf{m} \in \mathcal{G}(p, n)$ and $\mathbf{m}_1 \in U_{\mathbf{m}}$, we have*

$$\text{Exp}_{\mathbf{m}} \circ \text{Log}_{\mathbf{m}}(\mathbf{m}_1) = \mathbf{m}_1$$

Proof. We follow here the same ideas as the ones in [45, Theorem 2.3.36]. Take first two orthonormal basis for \mathbf{m}, \mathbf{m}_1 and write \mathbf{Y}, \mathbf{Y}_1 the corresponding matrices. Then from (9) we have

$$\text{Log}_{\mathbf{m}}(\mathbf{m}_1) = d\pi_{\mathbf{Y}} \cdot (\mathbf{U} \arctan(\boldsymbol{\Sigma}) \mathbf{V}^T)$$

with

$$\mathbf{Y}_1 (\mathbf{Y}^T \mathbf{Y}_1)^{-1} - \mathbf{Y} = \mathbf{U} \boldsymbol{\Sigma} \mathbf{V}^T$$

From (4) we thus have

$$\text{Exp}_{\mathbf{m}} \circ \text{Log}_{\mathbf{m}}(\mathbf{m}_1) = \pi (\mathbf{Y} \mathbf{V} \cos(\arctan(\boldsymbol{\Sigma})) + \mathbf{U} \sin(\arctan(\boldsymbol{\Sigma})))$$

where $\mathbf{Q} := \cos(\arctan(\boldsymbol{\Sigma}))$ is some invertible matrix and

$$\sin(\arctan(\boldsymbol{\Sigma})) = \boldsymbol{\Sigma} \mathbf{Q}$$

so that

$$\begin{aligned} \mathbf{Y} \mathbf{V} \cos(\arctan(\boldsymbol{\Sigma})) + \mathbf{U} \sin(\arctan(\boldsymbol{\Sigma})) &= \mathbf{Y} \mathbf{V} \mathbf{Q} + \mathbf{U} \boldsymbol{\Sigma} \mathbf{Q} = (\mathbf{Y} \mathbf{V} + \mathbf{U} \boldsymbol{\Sigma}) \mathbf{Q} \\ &= \left(\mathbf{Y} \mathbf{V} + \mathbf{Y}_1 (\mathbf{Y}^T \mathbf{Y}_1)^{-1} \mathbf{V} - \mathbf{Y} \mathbf{V} \right) \mathbf{Q} \\ &= \mathbf{Y}_1 (\mathbf{Y}^T \mathbf{Y}_1)^{-1} \mathbf{V} \mathbf{Q} \end{aligned}$$

where $(\mathbf{Y}^T \mathbf{Y}_1)^{-1} \mathbf{V} \mathbf{Q}$ is an invertible matrix and then

$$\pi (\mathbf{Y} \mathbf{V} \cos(\arctan(\boldsymbol{\Sigma})) + \mathbf{U} \sin(\arctan(\boldsymbol{\Sigma}))) = \pi(\mathbf{Y}_1) = \mathbf{m}_1$$

which concludes the proof. \square

Remark 4.11. Lemma 4.10 doesn't mean that the Grassmannian logarithmic map $\text{Log}_{\mathbf{m}}$ from Definition 4.9 is the inverse map of the exponential map $\text{Exp}_{\mathbf{m}}$ defined on all the tangent space $T_{\mathbf{m}}\mathcal{G}(p, n)$. For instance, we cannot have

$$\text{Log}_{\mathbf{m}} \circ \text{Exp}_{\mathbf{m}}(v) = v$$

for all $v \in T_{\mathbf{m}}\mathcal{G}(p, n)$. Indeed, taking any v such that $\|v\| > \text{diam}$ (given by (6)), such relation is impossible.

5. ROM Adaptation Based on Interpolation in Grassmann Manifolds

Take back here the N points $\{\mathbf{m}_i\}_{i=1}^N$ in the Grassmannian manifold $\mathcal{G}(n, p)$, all obtained from the ROMs of the snapshot matrices (as detailed in [section 3](#)). The goal here is to obtain an interpolation of a snapshot matrix associated with a new target point $\tilde{\lambda}$. To do so, we can for instance follow [\[32\]](#): the idea is to consider *normal coordinates* [\[13\]](#) in a neighborhood \mathcal{U}_0 of some base point $\mathbf{m}_0 \in \{\mathbf{m}_1, \dots, \mathbf{m}_N\}$, given by the exponential map $\text{Exp}_{\mathbf{m}_0}$ (see [Definition 4.5](#)).

Of course, the map

$$\phi_0 := (\text{Exp}_{\mathbf{m}_0})|_{\mathcal{U}_0} \subset T_{\mathbf{m}_0}\mathcal{G}(n, p) : \mathcal{U}_0 \longrightarrow \phi_0(\mathcal{U}_0) \subset \mathcal{G}(n, p)$$

has to be a *diffeomorphism*, and assumption $\mathbf{m}_i \in \phi_0(\mathcal{U}_0)$ for $i = 1, \dots, N$ should be made. Under these assumptions, let define

$$v_i := \phi_0^{-1}(\mathbf{m}_i) \in T_{\mathbf{m}_0}\mathcal{G}(n, p)$$

and let use classical interpolation (as the Lagrange interpolation) to obtain a new vector $\tilde{v} \in T_{\mathbf{m}_0}\mathcal{G}(n, p)$ associated to the target point $\tilde{\lambda}$. The interpolated point is finally given by:

$$\tilde{\mathbf{m}} := \phi_0(\tilde{v}).$$

Remark 5.1. To be sure the restricted Exponential map is a diffeomorphism, we can consider the injectivity radius (see [Theorem 4.8](#)) and consider only the points \mathbf{m}_i such that

$$d(\mathbf{m}_0, \mathbf{m}_i) \leq \frac{\pi}{2}$$

Nevertheless, we notice in all our cases that $\text{Log}_{\mathbf{m}_0}(\mathbf{m}_i)$ could be computed, even outside the injectivity radius (see [Appendix B](#)), so we could always obtain vectors $v_i \in T_{\mathbf{m}_0}\mathcal{G}(n, p)$, and thus an interpolated vector \tilde{v} . We have to be aware that in those case, we don't know what can happen, as we can have a loose of injectivity (see [Example 5.2](#)).

Example 5.2. The case of a cylinder $\mathcal{C} := \mathbb{S}^1 \times]-6; 6[\subset \mathbb{R}^3$ (where \mathbb{S}^1 is the first dimensional circle) can easily illustrate the situation of loose of injectivity. Taking $A(1, 0, 0) \in \mathcal{C}$ and $T_A\mathcal{C} = \mathbb{R}^2$, the exponential map is simply given by

$$\text{Exp}_A : v = (\theta, z) \in \mathbb{R}^2 \mapsto \text{Exp}_{A_0}(v) = (\cos(\theta), \sin(\theta), z)$$

where it is easy to check that the injectivity radius is π . Now, taking $B = (-1, 0, 0) \in \mathcal{C}$ and $U := (\mathbb{S}^1 - B) \times] - 6; 6[$ we can define

$$\text{Log}_A : M \in U \mapsto (\theta, z) \in] - \pi; \pi[\times \mathbb{R}, \quad M = (\cos(\theta), \sin(\theta), z)$$

so that $\text{Exp}_A \circ \text{Log}_A(M) = M$ for all $M \in U$. Note here that the open subset U is the *cut-locus* [13] of the point A .

Let consider the helix curve

$$\varphi(t) := (\cos(t), \sin(t), t), \quad t \in] - 1; 5[$$

and take four points

$$A_0 := \varphi(0) = 1, \quad A_1 := \varphi\left(-\frac{\pi}{6}\right), \quad A_2 := \varphi\left(\frac{5\pi}{6}\right), \quad A_3 := \varphi\left(\frac{4\pi}{3}\right)$$

so we can compute the associated vectors on $T_A\mathcal{C}$

$$v_i = \text{Log}_A(A_i)$$

and the loose of injectivity of the exponential map translates into a discontinuity from v_2 to v_3 (see Figure 2).

5.1. Lagrange Interpolation

Considering the velocities $v_i \in \mathcal{T}_{\mathbf{m}_0}\mathcal{G}(p, n)$ ($i = 1, \dots, N$), the Lagrange polynomials are used for the interpolated velocity \tilde{v} , given by:

$$\tilde{v} = \sum_{i=1}^N \prod_{i \neq j} \frac{\tilde{\lambda} - \lambda_j}{\lambda_i - \lambda_j} v_i \tag{10}$$

Remark 5.3. For explicit computation, let first consider $\mathbf{Y}_0 \in \pi^{-1}(\mathbf{m}_0)$ (see (1)) and define \mathbf{Z}_i to be the horizontal lift associated to v_i (see (2)). Then we define

$$\tilde{\mathbf{Z}} = \sum_{i=1}^N \prod_{i \neq j} \frac{\tilde{\lambda} - \lambda_j}{\lambda_i - \lambda_j} \mathbf{Z}_i$$

corresponding to \tilde{v} .

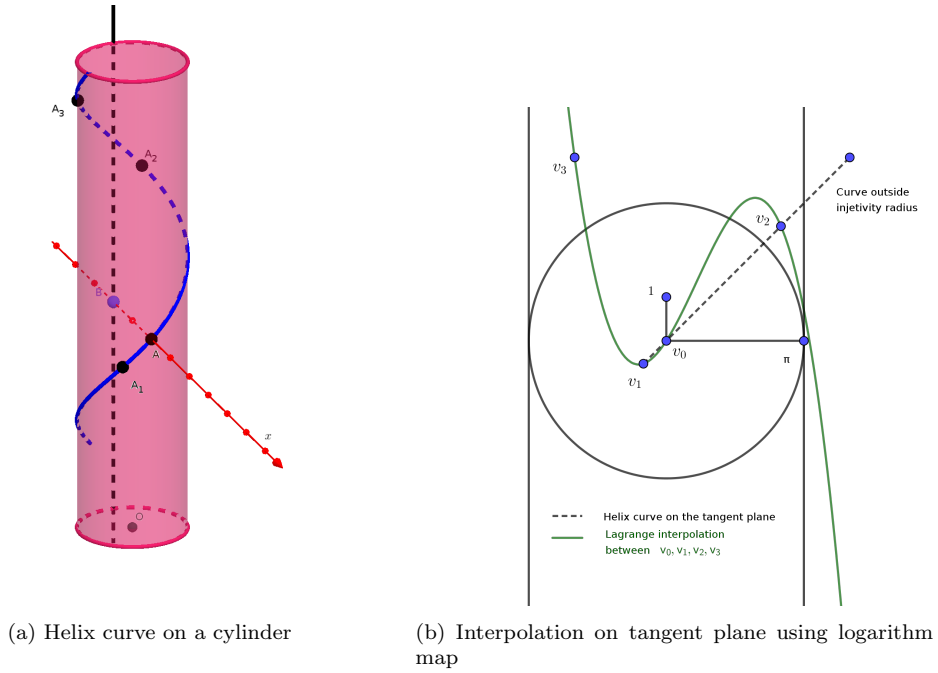


Figure 2: Interpolation of points on helix curve on a cylinder.

6. Application to Hyperelasticity

6.1. Kinematics of Continuum Mechanics Framework

Let $\Omega_0 \subset R^3$ and $\Omega \subset R^3$ represent the reference and the current configurations of a body, parameterized in \mathbf{X} and in \mathbf{x} , respectively. The non-linear deformation map $\varphi : \Omega_0 \rightarrow \Omega$ at time t , transforms the referential (material) position \mathbf{X} into the related current (spacial) position $\mathbf{x} = \varphi(\mathbf{X}, t)$. The deformation gradient \mathbf{F} is defined by

$$\mathbf{F} := \nabla \varphi(\mathbf{X}) = \frac{\partial \varphi(\mathbf{X})}{\partial \mathbf{X}} = \frac{\partial \mathbf{x}}{\partial \mathbf{X}} \quad (11)$$

with the Jacobian $J(\mathbf{X}) = \det(\mathbf{F}) > 0$ (volume ratio). The right and left Cauchy-Green tensors are defined as $\mathbf{C} = \mathbf{F}^T \mathbf{F}$ and $\mathbf{B} = \mathbf{F} \mathbf{F}^T$, respectively.

The three principal invariants of \mathbf{C} which are identical to those of \mathbf{B} are defined as

$$I_1 = \text{tr}(\mathbf{C}), \quad I_2 = \frac{1}{2}[(\text{tr}(\mathbf{C}))^2 - \text{tr}(\mathbf{C}^2)], \quad I_3 = \det(\mathbf{C}). \quad (12)$$

6.2. Incompressible Transverse Isotropic Material

A material with one family of fibers is considered where the stress at a material point depends not only on the deformation gradient \mathbf{F} but also on the fiber direction. The fibers are modelled by a *flow* [13] obtained from some unit vector field \mathbf{a}_0 on Ω_0 . The direction of a fiber at point $\mathbf{X} \in \Omega_0$ is thus obtained by the unit vector $\mathbf{a}_0(\mathbf{X})$, $|\mathbf{a}_0| = 1$.

Note that the unit vector field \mathbf{a}_0 induces a unit vector field \mathbf{a} on current configuration Ω defined by

$$\mathbf{F}(\mathbf{X})\mathbf{a}_0(\mathbf{X}) = \alpha\mathbf{a}(\mathbf{x})$$

where the length changes of the fibers along its direction \mathbf{a}_0 is determined by the stretch α as the ratio between the current and the reference configuration.

Consequently, since $|\mathbf{a}| = 1$, we can define the square of the stretch α following the symmetries of the deformation gradient

$$\alpha^2 = \mathbf{a}_0\mathbf{F}^T\mathbf{F}\mathbf{a}_0 = \mathbf{a}_0\mathbf{C}\mathbf{a}_0.$$

6.3. Linearization of the principle of internal virtual work in the spatial description

The linearization of the internal virtual work in the spatial description reads (see Section 8.4 in [25])

$$D_{\Delta\mathbf{u}}\delta W_{int}(\mathbf{u}, \delta\mathbf{u}) = \int_{\Omega} (\text{grad}\delta\mathbf{u} : \mathbb{c} : \text{grad}\Delta\mathbf{u} + \text{grad}\delta\mathbf{u} : \text{grad}\Delta\mathbf{u} \boldsymbol{\sigma}) dv \quad (13)$$

or in index notation (with Einstein convention on repeated indices),

$$D_{\Delta\mathbf{u}}\delta W_{int}(\mathbf{u}, \delta\mathbf{u}) = \int_{\Omega} \frac{\partial\delta u_a}{\partial x_b} (\delta_{ac}\sigma_{bd} + \mathbb{c}_{abcd}) \frac{\partial\Delta u_c}{\partial x_d} dv \quad (14)$$

where the term $\delta_{ac}\sigma_{bd} + \mathbb{c}_{abcd}$ is the effective elasticity tensor in the spatial description. The term $\delta_{ac}\sigma_{bd}$ corresponds to the geometrical stress contribution to linearization (initial stress contribution at every increment) whereas \mathbb{c}_{abcd} represents the material contribution to linearization. The elasticity tensor \mathbb{c}_{abcd} in the spatial description is derived from the push-forward of the linearized second Piola-Kirchhoff stress tensor which yields the linearized Kirchhoff stress tensor $\Delta\boldsymbol{\tau}$ from relation

$$\Delta\boldsymbol{\tau} = J\mathbb{c} : \text{grad}\Delta\mathbf{u} \quad (15)$$

Replacing the direction $\Delta \mathbf{u}$ of the directional derivative with the velocity vector \mathbf{v} , $\Delta \boldsymbol{\tau}$ and $\text{grad} \Delta \mathbf{u}$ result in the Lie time derivative $\mathcal{L}_v(\boldsymbol{\tau})$ of $\boldsymbol{\tau}$ and the spatial velocity gradient $\mathbf{l} = \dot{\mathbf{F}}\mathbf{F}^{-1}$, respectively. Again, using the minor symmetries of \mathfrak{c} , the following relation can be written

$$\mathcal{L}_v(\boldsymbol{\tau}) = \text{Oldr}(\boldsymbol{\tau}) = \dot{\boldsymbol{\tau}} - \mathbf{l}\boldsymbol{\tau} - \boldsymbol{\tau}\mathbf{l}^T = J\mathfrak{c} : \mathbf{d} \quad (16)$$

where $\text{Oldr}(\boldsymbol{\tau})$ denotes the objective Oldroyd stress rate (convected rate) of the contravariant Kirchhoff stress tensor $\boldsymbol{\tau}$ and $\mathbf{d} = \text{sym}(\mathbf{l})$ (symmetric part of \mathbf{l}) the rate of the deformation tensor. At this point we have to recall that for structural elements (shells, membranes, beams, trusses) Abaqus/Standard uses the elasticity tensor related to the Green-Naghdi objective rate (see [Appendix A](#)). The detailed constitutive model used here is given in [30].

7. Numerical Investigations

The objective of this section is to investigate the POD basis interpolation accuracy in two examples in hyperelasticity.

7.1. Abaqus implementation of POD-ROM approximations

To implement the interpolated spatial POD basis into a commercial code, a non intrusive approach is used. Specifically, the multi-point constraint equations in Abaqus [40] are used to construct the ROM model. A linear multi-point constraint requires that a linear combination of nodal variables is equal to zero:

$$A_1 u_i^P + A_2 u_j^Q + \dots + A_N u_k^R = 0 \quad (17)$$

where u_i^P is the nodal variable at node P , degree of freedom i and A_i , ($i = 1, \dots, N$) are coefficients that define the relative motion of the nodes. In Abaqus/Standard the first nodal variable specified (u_i^P corresponding to A_1) will be eliminated to impose the constraint. In addition, the coefficient A_1 should not be set to zero. For the construction of the reduced order model, p reference points are created corresponding to the total number of POD modes (arbitrary positioned in space). These reference points are used to define the constraint equations for introducing the spatial POD modes and to assign the extra degrees of freedom corresponding to the unknown time

variables. Thus, the interpolated spatial basis $\tilde{\mathbf{m}} := \text{span}(\tilde{\phi}_1, \dots, \tilde{\phi}_p)$ on $\mathcal{G}(p, n)$ is imposed to the linear constraint equations as follows:

$$u(x_l, t, \tilde{\lambda}) - \sum_{h=1}^p \tilde{\phi}_h(x_l) \psi_h(t) = 0 \quad (18)$$

where x_l , ($l = 1, \dots, N_s$) is related to the nodal point positions, $\tilde{\phi}_h(x_l)$ represent the associated spatial POD h -mode for x_l , and $\psi_h(t)$ is the time variable assigned to the reference point h that has to be determined. Note also that the system of equations defined in (18) has to be generated for each degree of freedom.

Remark 7.1. In fact this is not a standard POD-Galerkin approach since we are not projecting the linearized system of equations onto the interpolated spatial POD basis. But it serves to asses the accuracy of the ROM FEM model which is constructed by the interpolated POD basis.

7.2. Inflation of a spherical balloon

The first benchmark model concerns the inflation of an anisotropic spherical balloon considering material anisotropy as a parameter. The sphere has an initial radius of $R = 10$, thickness $h = 0.5$ and is loaded by an internal hydrostatic pressure of $P = 40$ (no units). Analysis is performed on an octant S_0 of the sphere using plane symmetry boundary conditions, as depicted in Figure 3 where three radial points $A(R, 0, 0)$, $B(0, R, 0)$ and $C(0, 0, R)$ are defined on each axis, respectively. Three-node shell elements (S3R) are used for the mesh. A total number of 514 elements are generated with 228 nodes. The constitutive behavior is implemented in Abaqus/Standard with a user-defined subroutine (UMAT) [40].

Remark 7.2. The fiber orientation has to be defined on each point $M \in S_0$ using an orthonormal basis of the tangent plane $T_M S_0$, which has to be specified.

The choice made in Abaqus is to consider first an outward normal $\mathbf{n}(M)$ to this tangent plane and then a first vector $\mathbf{E}_1(M)$ as the orthogonal projection (normalized) of $\mathbf{e}_1 := (1, 0, 0)$ onto $T_M S_0$. The second unit vector is the cross product $\mathbf{E}_2(M) := \mathbf{n}(M) \wedge \mathbf{E}_1(M)$.

Explicit fiber orientations on the octant

Let make now an explicit definition of the fiber orientations, with parameter some angle θ using local basis $\mathbf{E}_1(M)$, $\mathbf{E}_2(M)$ of the tangent plane $T_M S_0$

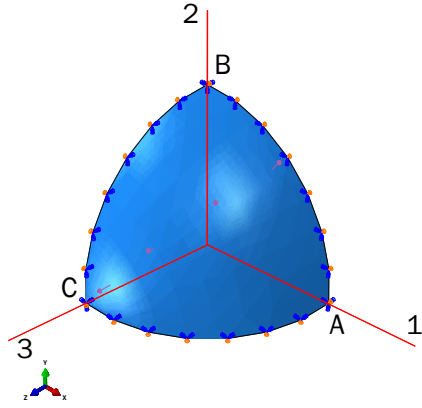


Figure 3: Geometry of an octant S_0 of a spherical balloon made of transversely isotropic material. Three radial points A, B and C are defined on axis 1,2 and 3, respectively; plane symmetry boundary conditions are used.

as explained in Remark 7.2. More specifically, take

$$M = (\cos(u) \sin(v), \sin(u) \sin(v), \cos(v)) \in S_0, \quad (u, v) \in \left] 0; \frac{\pi}{2} \right[\times \left] 0; \frac{\pi}{2} \right[$$

and then define

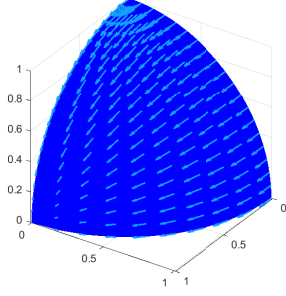
$$\mathbf{E}_1(M) := \frac{\mathbf{X}^h}{\|\mathbf{X}^h\|}, \quad \mathbf{X}^h := \begin{pmatrix} 1 - \cos^2(u) \sin^2(v) \\ -\sin(u) \cos(u) \sin^2(v) \\ -\cos(u) \sin(v) \cos(v) \end{pmatrix},$$

$$\mathbf{E}_2(M) := \mathbf{n}(M) \wedge \mathbf{E}_1(M).$$

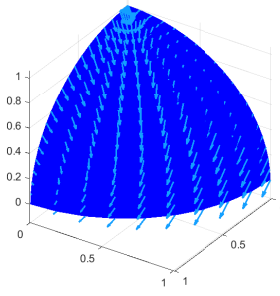
Note here that the vector \mathbf{X}^h corresponds to the orthogonal projection of the vector $(1, 0, 0)$ onto the tangent plane $T_M S_0$.

Finally, the unit vector defining the fiber orientation is given by (see Figure 4 for some examples).

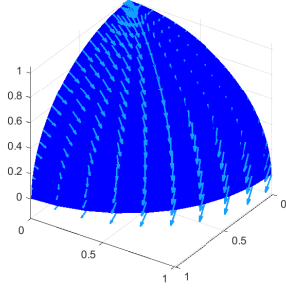
$$\mathbf{a}_0(\theta) := \cos(\theta) \mathbf{E}_1(M) + \sin(\theta) \mathbf{E}_2(M)$$



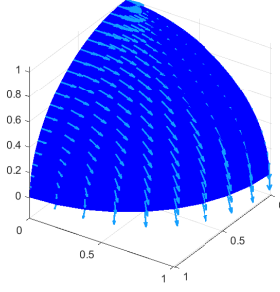
(a) Fibers orientation with $\theta = 0$ degree



(b) Fibers orientation with $\theta = 45$ degree



(c) Fibers orientation with $\theta = 60$ degree



(d) Fibers orientation with $\theta = 90$ degree

Figure 4: Different fibers on the sphere.

Model for strain energy function

For a homogeneous transversely isotropic non-linear material, let consider a free energy function that depends only on two invariants (I_1, I_4)

$$\Psi = \Psi (I_1(\mathbf{C}), I_4(\mathbf{C}, \mathbf{a}_0))$$

where $I_1 = \text{tr}(\mathbf{C})$, while

$$I_4 = \mathbf{a}_0 \mathbf{C} \mathbf{a}_0, \quad (19)$$

is the invariant related to anisotropy. Since we assume incompressibility of the isotropic matrix material, i.e., $I_3 = 1$, the free energy is enhanced by an indeterminate Lagrange multiplier p which is identified as a reaction pressure

$$\Psi = \Psi[I_1(\mathbf{C}), I_4(\mathbf{C}, \mathbf{a}_0)] + p(I_3 - 1).$$

The specific model used here is developed for membranous or thin shell-like sheets considering a plane stress state throughout the sheet [30]. Following the method of Humphrey [14] which is based on a derivation by

Spencer [5], the strain energy function is defined as

$$\Psi(I_1, I_4) := c_0(\exp(Q) - 1), \quad Q := c_1(I_1 - 3)^2 + c_2(I_4 - 1)^2 \quad (20)$$

where $c_i, i = 0, 1, 2$ are material parameters defined as: $c_0 = 86.1$, $c_1 = 0.0059$ and $c_2 = 0.031$ (dimensionless).

Remark 7.3. This model introduces an inherent constitutive coupling between the isotropic and anisotropic material response. In order to avoid non-physical behavior of soft biological tissues, the related strain-energy function must be polyconvex. It can be shown that polyconvexity of a (continuous) strain-energy function implies that the corresponding acoustic tensor is elliptic for all deformations, which means from the physical point of view that only real wave speeds occur; then the material is said to be stable. There exists a vast literature on polyconvexity, a term introduced by Ball [8]. In (20), the anisotropic term $c_2(I_4 - 1)^2$ is activated only when $I_4 \geq 1$ (the actual fiber stretches are greater than unity).

Moreover, as discussed in [23], the constitutive description based on (20) is limited to deformations in which the in-plane strains are positive, or tensile and is not able to incorporate the behavior of the structure in compression. Due to the membrane-like geometry of the structure, it is unlikely to support compressive strains without buckling. This limitation extends to the issue of bending stiffness, which is neglected in this model.

Snapshot matrices and error norms

In what follows, the training points are represented by the variable angle $\lambda = \theta$. FEM simulations are performed in Abaqus/Standard for the training points $\lambda_i \in \Lambda_s = \{0, 45, 50, 60, 85, 90\}$ whereas the target point for the interpolation is set to $\lambda = 75$. Because of this choice, it is natural to constraint the training set to $\Lambda_t = \{50, 60, 85, 90\}$ for the interpolation (see Figure 5 for some FEM results). For each parametric simulation, a sequence of uniform time snapshots is extracted from the model database. From the discretization of the space-time fields (displacement/rotation), the snapshot matrices $\mathbf{S}(\lambda_i)$ of size $(n = 1728) \times (N_t = 1000)$ are formed.

The eigenvalue spectrum of the matrices $\mathbf{S}(\lambda_i)$ corresponding to training points $\lambda_i \in \Lambda_t$ is shown in a log-log scale in Figure 6. The condition number of the matrices is of the order of $1.0e + 10$. Notice that the distance between the first and the second eigenvalue is of two orders of magnitude.

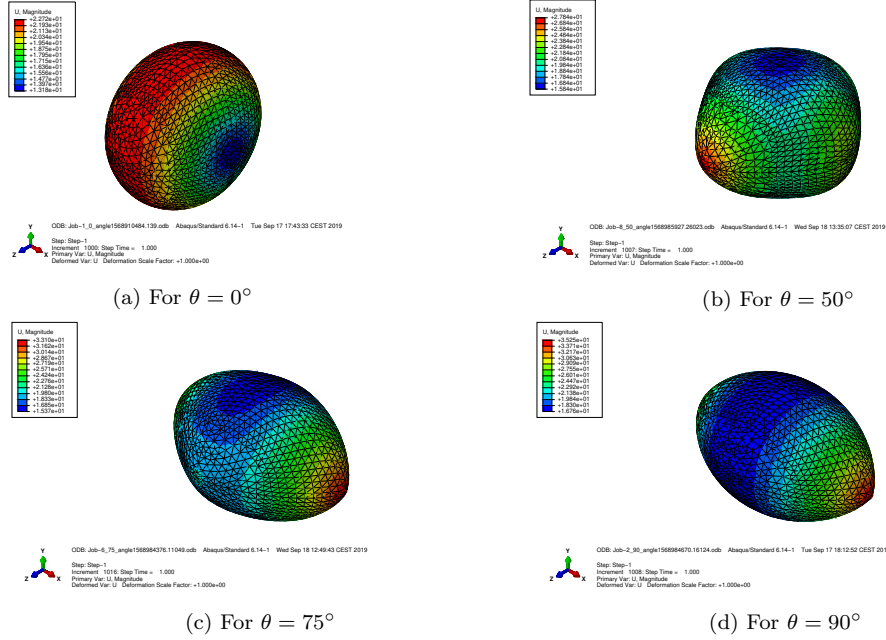


Figure 5: Inflation modes of the benchmark anisotropic spherical balloon after reconstruction of the complete balloon using the plane symmetries conditions at the boundaries of the octant S_0 .

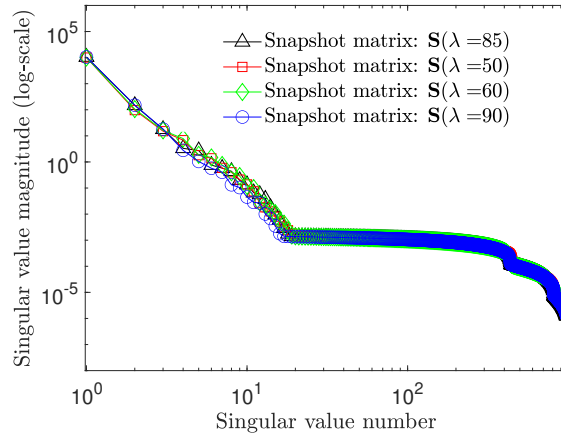


Figure 6: The eigenvalue spectrum of snapshot matrices \mathbf{S}_i corresponding to training points $\lambda_i = 50, 60, 85, 90$.

To quantify the accuracy of the interpolation, the relative L_2 -error norm (in time) for a given target point $\tilde{\lambda}$ is evaluated with respect to the high-fidelity FEM solution. Using the interpolated and the HF-FEM snapshot matrices $\tilde{\mathbf{S}}$ and \mathbf{S}^{FEM} , respectively, the following error measure is defined at each time snapshot

$$e_{L_2}(\tilde{\mathbf{S}}) = \frac{\|\tilde{\mathbf{u}}_i - \mathbf{u}_i^{\text{FEM}}\|_{L_2}}{\|\mathbf{u}_i^{\text{FEM}}\|_{L_2}}, \quad i = 1, \dots, N_t \quad (21)$$

In addition, the relative Frobenius error norm represents a global error measure which considers the error in the full time interval of the time steps

$$e_F(\tilde{\mathbf{S}}) = \|\tilde{\mathbf{S}} - \mathbf{S}^{\text{FEM}}\|_F / \|\mathbf{S}^{\text{FEM}}\|_F \quad (22)$$

First, the accuracy of POD ROM-FEM is assessed using the Lagrange interpolation. Using the linear constraint equations defined in (18), p reference points (for each POD mode) are created to assign the spatial POD basis representing the interpolated subspace $\tilde{\mathbf{m}} \in \mathcal{G}(p, n)$ and the unknown time variables. The total number of equations of the ROM-FEM model is $6 \times p$ while the total number of equations of the corresponding HF-FEM model is $288 \times 6 = 1728$. Figure 7 and Figure 8 show the relative L_2 -error norm $e_{L_2}(\tilde{\mathbf{S}})$ and the Frobenius error norm $e_F(\tilde{\mathbf{S}})$ for the target point $\tilde{\lambda}$ of the ROM-FEM solution (constructed from the interpolated p spatial modes) and the high fidelity FEM counterpart solution.

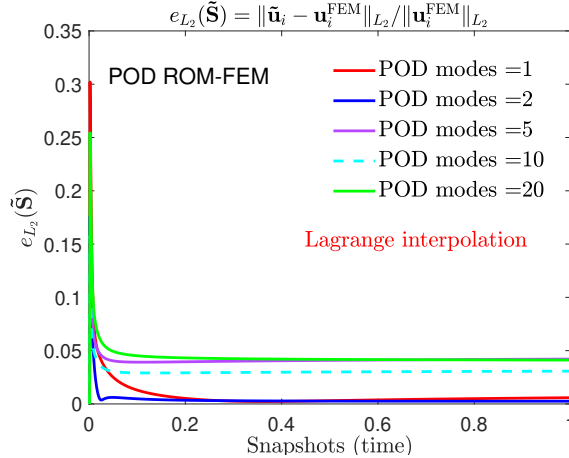


Figure 7: Relative L_2 -error norm $e_{L_2}(\tilde{\mathbf{S}})$ against the number of POD vectors for the POD ROM-FEM; target point: $\tilde{\mathbf{m}}(\lambda = 75)$.

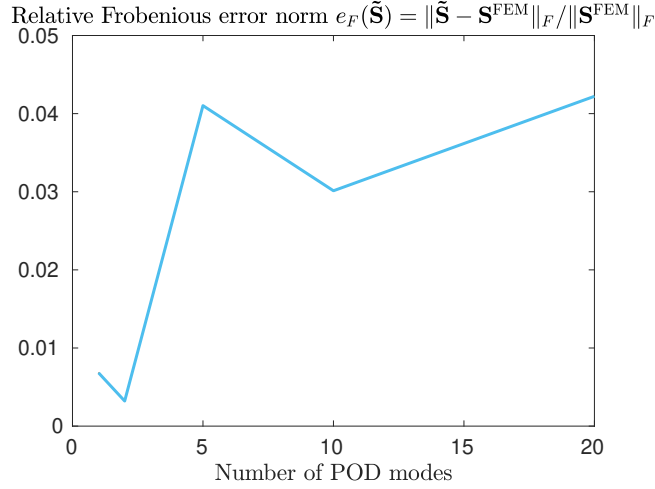


Figure 8: Relative Frobenious error norm against the number of POD vectors for the POD ROM-FEM; target point: $\tilde{\mathbf{m}}(\lambda = 75)$.

Remark 7.4. Unexpectedly, the error is minimum for $p = 2$ POD modes and increases by introducing additional modes, a result which is contradicting the expected improvement of the solution with the number of vectors. The non-monotonous decrease and the random oscillations can be attributed to the independence between the p -dimensional solutions on the Grassmann manifolds associated with the Grassmannian imbedding theorem (Theorem 13) [4].

Additionally, the position vector error norm $e_{\mathbf{x}} = \|\tilde{\mathbf{x}}(t) - \mathbf{x}^{\text{FEM}}(t)\|_{L_2}$ at the nodal points is computed for $p = 1, 2, 5$ and 10 POD modes. Figure 9 and Figure 10 present the local error at the increment state $t = 0.002$ and at the final increment state $t = 1$, respectively. In general, different patterns of the spatial error distribution can be observed with respect to the number of POD modes. In the majority of cases, the maximum error is located at the boundary points of the octant S_0 of the sphere where the plane symmetries are imposed and at points of maximum displacement. Again, it is evident that the error is not decreasing with the number of POD vectors.

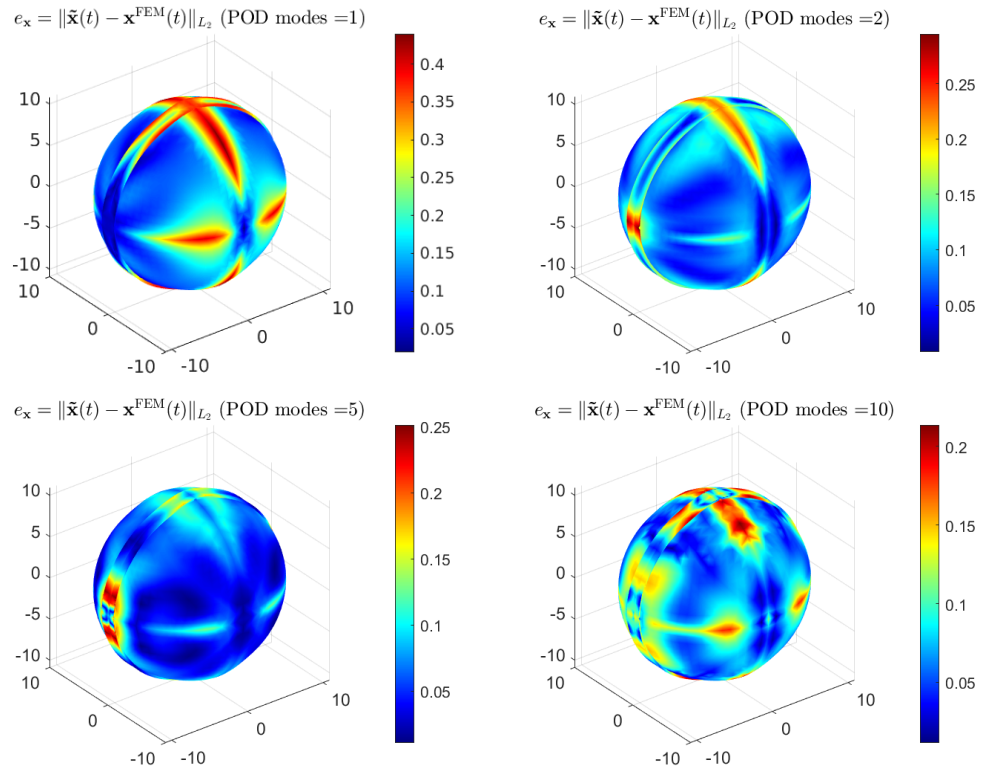


Figure 9: POD ROM-FEM; Position vector error norm $e_{\mathbf{x}} = \|\tilde{\mathbf{x}}(t) - \mathbf{x}^{\text{FEM}}(t)\|_{L_2}$ at the nodal points at state $t = 0.002$ for POD modes $p = \{1, 2, 5, 10\}$; target point: $\tilde{\mathbf{m}}(\lambda = 75)$.

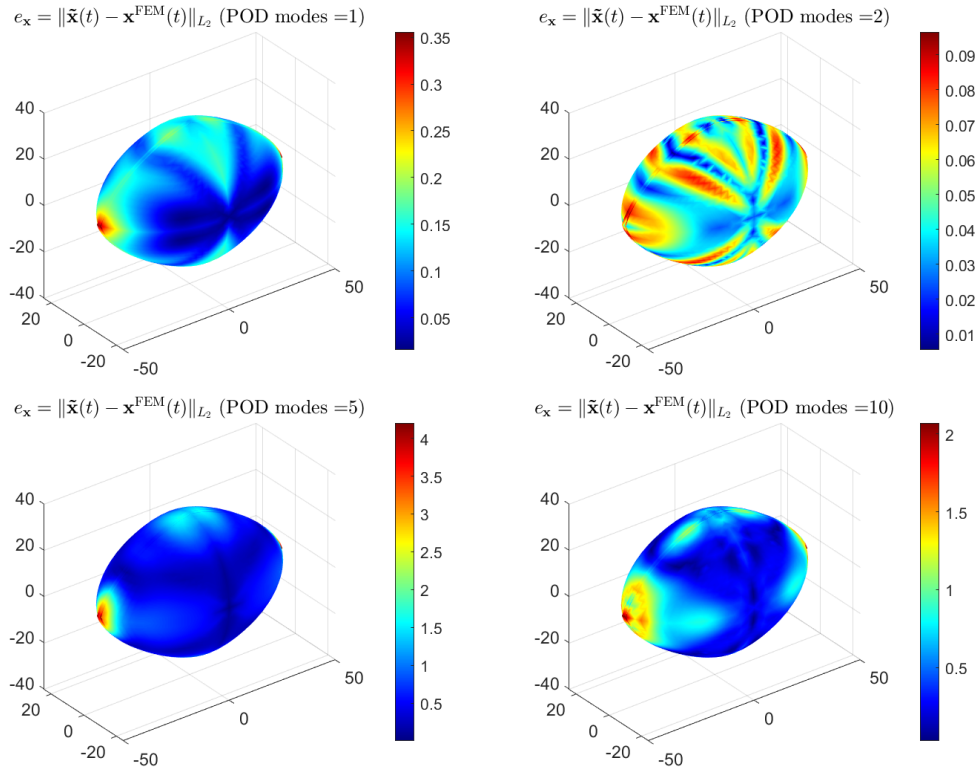


Figure 10: POD ROM-FEM; Position vector error norm $e_{\mathbf{x}} = \|\tilde{\mathbf{x}}(t) - \mathbf{x}^{\text{FEM}}(t)\|_{L_2}$ at the nodal points at state $t = 1$ for POD modes $p = \{1, 2, 5, 10\}$; target point: $\tilde{\mathbf{m}}(\lambda = 75)$.

Finally, Figure 11 shows the time-displacement histories for the radial points A, B and C on the spherical balloon for the POD ROM-FEM compared against its high fidelity counterpart solution using the first POD mode. It can be observed that the interpolated ROM-FEM solution delivers good accuracy and is accurate enough to predict the anisotropic balloon inflation at the target condition.

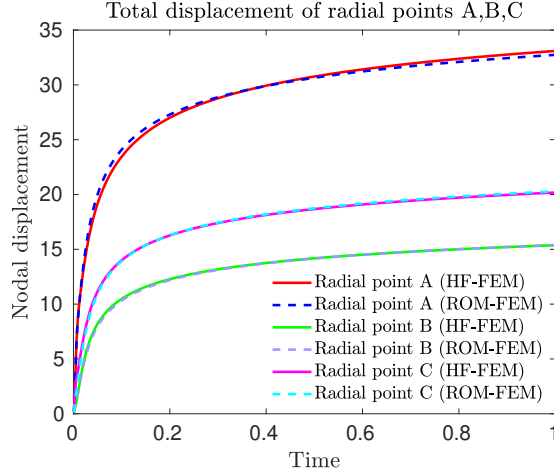


Figure 11: POD ROM-FEM using Lagrange interpolation; comparison of the displacement of radial points A,B and C against the high-fidelity FEM solution; training points: $\mathbf{m}_0(\lambda = 85)$ (reference point); $\mathbf{m}_1(\lambda = 50)$; $\mathbf{m}_2(\lambda = 60)$; $\mathbf{m}_3(\lambda = 90)$; target point: $\tilde{\mathbf{m}}(\lambda = 75)$; POD modes $p = 1$.

7.3. Hyperelastic structure with multiple components

In what follows, pMOR is investigated for a structural model considering the material stiffness as a parameter. The model consists of two basic components: a plane shell section which is connected with truss elements (non-symmetrically) (see Figure 12). The plane geometry has dimensions 20×20 (mm), a constant thickness of 0.5 mm and is meshed with rectangular shells (S4). The hyperelastic model defined in (20) (UMAT) is assigned to the plane section in which the fiber orientations are aligned with the x-axis. The following parameters are used: $c_0 = 0.0520$ (kPa), $c_1 = 4.63$ and $c_2 = 22.6$. The truss elements is of type T3D2 with a cross section area of 1 mm^2 . For these elements, an isotropic incompressible hyperelastic material model is implemented into the Abaqus/Standard subroutine UHYPER [40]. The material model is derived from the following strain-energy function

$$U = \alpha_1(\exp[\alpha_2(I_1 - 3)] - 1) \quad (23)$$

where α_1 and α_2 are material parameters defined as: $\alpha_1 = 0.0565$ kPa and α_2 is used for the parametric analysis. At the boundary of the plane section ($x = 0$) and at the foundations of the truss elements all degrees of freedom are set to zero. A constant hydrostatic pressure of 120 mmHg (0.016 MPa) is applied at the bottom of the plane section.

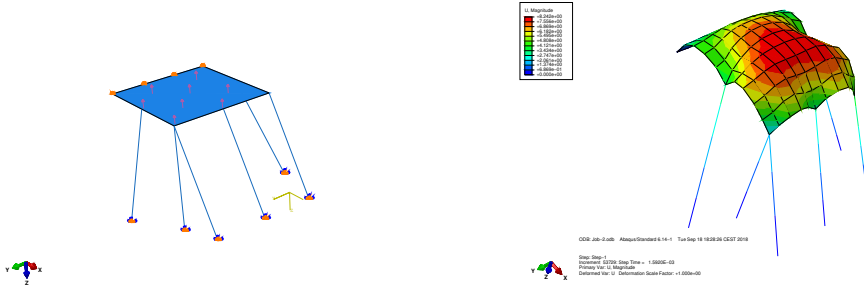


Figure 12: Geometry, boundary conditions and total displacement of the structural model.

Simulations are performed in Abaqus/Standard (Implicit). The following training points for the exponential parameter α_2 are selected which are represented by the variable $\lambda \in \{5, 10, 15, 20, 25, 30\}$. Figure 13 shows the second Piola-Kirchhoff stress-stretch curves for the associated parameter values which reveals a wide spectrum of stress values. For each parametric simulation, a sequence of snapshots uniformly distributed over time using an increment of $\Delta t = 0.001$ is extracted for all nodes of the plane structure from the model database. The space-time snapshot matrices $\mathbf{S}(\lambda_i) \in \mathbb{R}^{n \times N_t}$ of size $(n = 726) \times (N_t = 1000)$ are associated to nodal displacement and rotational fields. The following training points $\lambda_i \in \Lambda_t = \{15, 20, 25, 30\}$ are chosen for estimating the target point $\tilde{\lambda} = 17.5$. Then, the set of the low-dimensional POD basis is interpolated on the Grassmann manifold using Lagrange interpolation. POD ROM-FEM interpolation is compared against the high-fidelity FEM solution.

The eigenvalue spectrum of snapshot matrices \mathbf{S}_i corresponding to training points $\lambda_i \in \Lambda_t$ is shown in a log-log scale in Figure 14. It is evident that the distance between the first and the next two eigenvalues is in a range of one order of magnitude.

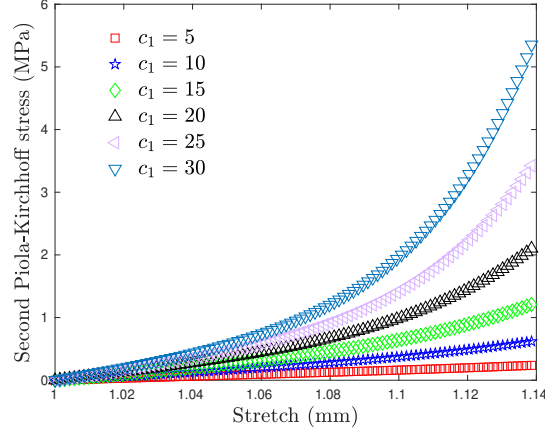


Figure 13: Second Piola-Kirchhoff stress vs stretch for the examined parameter range.

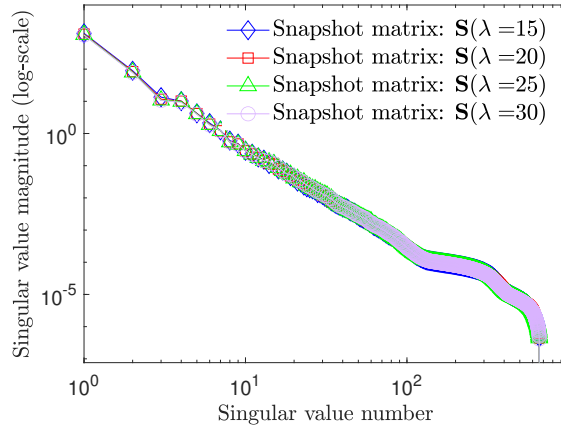


Figure 14: The eigenvalue spectrum of snapshot matrices \mathbf{S}_i corresponding to training points $\lambda_i = 15, 20, 25, 30$.

First, the application of the POD ROM-FEM is investigated. The interpolated spatial basis representing the subspace $\tilde{\mathbf{m}}$ on $\mathcal{G}(p, n)$ is introduced using the linear constraint equations (Section 7.1) in Abaqus to construct a low dimensional ROM FEM model associated to the target parametric point. For each low dimensional model corresponding to $p = 1, 2, 5, 10, 20$ modes, a number of $\{\text{RP}_h\}_{h=1}^p$ reference points are created to assign the interpolated spatial POD modes and the unknown time variables. Table 1 and Table 2

report in detail the degrees of freedom of the high fidelity and the reduced order FEM model using $p = 10$ POD modes, respectively. Clearly, at the ROM model, a reduction of the total number of equations by a factor ≈ 9.5 is obtained. Besides, the constraint of the degrees of freedom induced by the POD spatial modes enhance the stability and convergence of the ROM-FEM problem.

The accuracy of the POD ROM-FEM is assessed by comparing the relative L_2 -error norm $e_{L_2}(\tilde{\mathbf{S}})$ between the reduced order FEM and its directly high-fidelity computed counterpart solution with the number of POD modes, as shown in Figure 15. Opposite to the previous example, in this case, the error is decreasing by using more POD modes. Furthermore, Figure 16 shows a comparison of the approximated time histories of selected nodal total displacements for $p = 20$ modes against the high fidelity FEM solution. It is evident that all nodal time-histories are nearly identical.

Table 1: High Fidelity FEM

Element type	N. of elements	DOF	N. of nodes	Total DOF
S4	100	6	121	726
T3D2	6	3	12	36
N. of tie constraints				
6		3	6	18
N. of equations				744

Table 2: ROM-FEM

Element type	N. of elements	DOF	N. of nodes	Total DOF
-	-	6	10 (RP)	60
T3D2	6	3	12	36
N. of tie constraints				
6		3	6	18
N. of equations				78

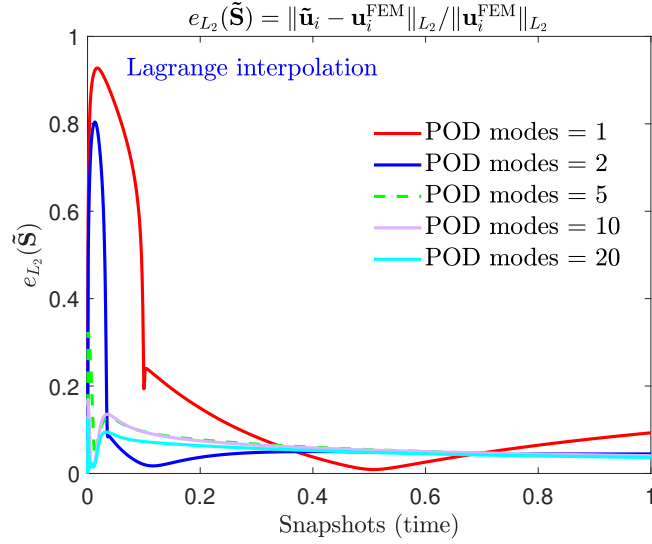


Figure 15: POD ROM-FEM; relative L_2 -error norm $e_{L_2}(\tilde{\mathbf{S}})$ against the number of POD vectors; target point: $\tilde{\mathbf{m}}(\lambda = 17.5)$; Lagrange interpolation.

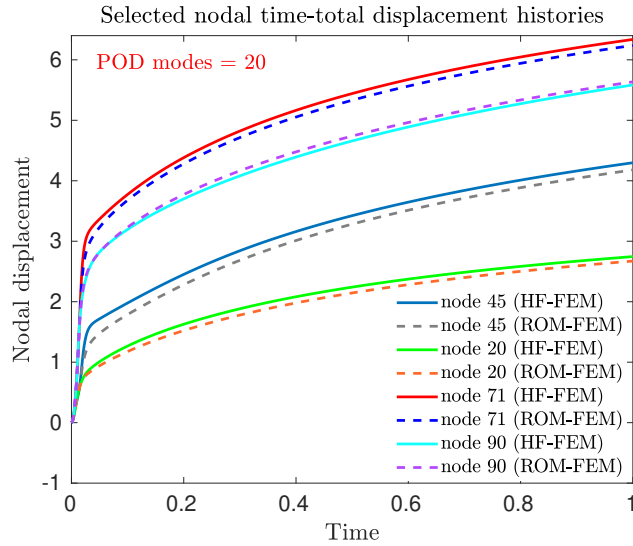


Figure 16: POD ROM-FEM; comparison of selected nodal time-displacement histories against the high-fidelity FEM solution; training points: $\mathbf{m}_0(\lambda = 15)$; $\mathbf{m}_1(\lambda = 20)$; $\mathbf{m}_2(\lambda = 25)$; $\mathbf{m}_3(\lambda = 30)$; target point: $\tilde{\mathbf{m}}(\lambda = 17.5)$; POD modes = 20.

8. Conclusions

A concrete mathematical approach for POD ROM basis interpolation on Grassmann manifolds for pMOR in hyperelasticity is presented. Special attention has been paid on the local maps on the Grassmann manifolds considering the logarithm and the exponential maps. The implication of the injectivity radius which defines the radius of the largest ball about the origin on the tangent plane that the exponential map is a diffeomorphism is highlighted together with the notion of the cut-locus. The loss of injectivity is clearly exhibited using an illustrative low dimensional example. Via a non-intrusive method, the target POD spatial basis is inserted in a commercial code to construct a ROM-FEM model. To this end, only the accuracy of interpolation is assessed against the high-fidelity FEM solution since the ROM model still embeds the high dimension. Different structural problems are used to evaluate the accuracy of the ROM FEM models constructed from the interpolated spatial POD basis. Numerical investigations of the error norms showed good accuracy in both numerical cases. It has to be remarked that the interpolated ROM FEM solutions associated to the p -dimensional POD basis for $p = 1, \dots, k$ are not connected. A direct consequence is the possible occurrence of a non-monotonic and spurious oscillatory behavior of the error norm with respect to the number of POD modes.

9. Acknowledgements

This work has been funded by DGA (“direction générale pour l’armement”, French ministry of defense) under the RAPID contract called “Innvivotech Tissus Mous” in partnership with BIOMODEX.

Appendix A. Derivation of the Green-Naghdi objective rate

Using the definitions of the Jaumman-Zaremba and the Green-Naghdi objective rates, the following relation holds

$$\text{GreeNag}(\boldsymbol{\tau}) = \text{Jaum}(\boldsymbol{\tau}) + (\mathbf{w} - \boldsymbol{\Omega})\boldsymbol{\tau} - \boldsymbol{\tau}(\mathbf{w} - \boldsymbol{\Omega}) \quad (\text{A.1})$$

where $\boldsymbol{\Omega} = \dot{\mathbf{R}}\mathbf{R}^T$, \mathbf{R} is the rotation tensor and \mathbf{w} is the spin tensor. Mehrabadi and Nemat-Nasser [12] (Appendix A. Derivation of 8.15) showed that it is possible to solve this equation explicitly for $(\mathbf{w} - \boldsymbol{\Omega})$ by repeatedly using the Cayley-Hamilton theorem; The end result is expressed as

$$\mathbf{w} - \boldsymbol{\Omega} = \mathbb{A}(\mathbf{v}) : \mathbf{d} \quad (\text{A.2})$$

where \mathbb{A} is a fourth-order tensor defined through eq.(7.3.12a) in Simo and Hughes [29] and \mathbf{v} denote the left spatial stretch tensor derived from the polar decomposition of the deformation gradient $\mathbf{F} = \mathbf{v}\mathbf{R}$.

$$\mathbb{A} : \mathbf{d} = \frac{1}{I_{1\mathbf{v}}I_{2\mathbf{v}} - I_{3\mathbf{v}}} \left(I_{1\mathbf{v}}^2(\mathbf{v}\mathbf{d} - \mathbf{d}\mathbf{v}) - I_{1\mathbf{v}}(\mathbf{B}\mathbf{d} - \mathbf{d}\mathbf{B}) + \mathbf{B}\mathbf{d}\mathbf{v} - \mathbf{v}\mathbf{d}\mathbf{B} \right) \quad (\text{A.3})$$

where

$$I_{1\mathbf{v}} = \text{tr}(\mathbf{v}), \quad I_{2\mathbf{v}} = \frac{1}{2} \left(\text{tr}(\mathbf{v})^2 - \text{tr}(\mathbf{v}^2) \right), \quad I_{3\mathbf{v}} = \det(\mathbf{v}) \quad (\text{A.4})$$

In index notation, \mathbb{A} is expressed as:

$$\begin{aligned} \Lambda_{ijkl} = & \frac{1}{I_{1\mathbf{v}}I_{2\mathbf{v}} - I_{3\mathbf{v}}} \left(I_{1\mathbf{v}}^2 \frac{1}{2} (\delta_{jl}v_{ik} + \delta_{jk}v_{il} - (\delta_{ik}v_{jl} + \delta_{il}v_{jk})) \right. \\ & - I_{1\mathbf{v}} \frac{1}{2} (\delta_{jl}B_{ik} + \delta_{jk}B_{il} - (\delta_{ik}B_{jl} + \delta_{il}B_{jk})) \\ & \left. + \frac{1}{2} (B_{ik}v_{lj} + B_{il}v_{kj} - (v_{ik}B_{lj} + v_{il}B_{kj})) \right) \quad (\text{A.5}) \end{aligned}$$

Note that \mathbb{A} does not have the major symmetries but possesses minor symmetry and skew symmetry

$$\Lambda_{ijkl} \neq \Lambda_{klij} \quad (\text{A.6})$$

$$\Lambda_{ijkl} = \Lambda_{ijlk} = -\Lambda_{jikl} \quad (\text{A.7})$$

The following terms of \mathbb{A} are equal to zero:

$$\Lambda_{1111} = \Lambda_{1122} = \Lambda_{1112} = \Lambda_{2211} = \Lambda_{2222} = \Lambda_{2212} = 0 \quad (\text{A.8})$$

Hence,

$$\text{GreeNag}(\boldsymbol{\tau}) = \mathbf{c}^{JZ} : \mathbf{d} + (\mathbb{A} : \mathbf{d})\boldsymbol{\tau} - \boldsymbol{\tau}(\mathbb{A} : \mathbf{d}) = \mathbf{c}^{GN} : \mathbf{d} \quad (\text{A.9})$$

or in index notation

$$\text{GreeNag}(\tau)_{ij} = [c_{ijkl}^{JZ} - \Lambda_{i\alpha kl}\tau_{\alpha j} + \tau_{i\alpha}\Lambda_{\alpha jkl}]d_{kl} = c_{ijkl}^{GN} : d_{kl} \quad (\text{A.10})$$

where the terms between the brackets yield the desired result, i.e. the components of the non-symmetric Green–Naghdi tangent moduli c_{ijkl}^{GN} . The lack of diagonal (major) symmetry of the elasticity tensor associated with the Green–Naghdi rate of the Kirchhoff stress has been pointed out as one of the drawbacks of this choice [29], as it implies that the stiffness matrices are non-symmetric, i.e.,

$$c_{ijkl}^{GN} - c_{klij}^{GN} \neq 0 \quad (\text{A.11})$$

Appendix B. Grassmannian distances and injectivity radius

The interpolation procedure given in [section 5](#) uses normal coordinates on Grassmann manifold. One main issue is that such manifold is not a vector space, but only looks like an open space of a vector space, *via* local charts. Normal coordinates use the exponential map (see [4.5](#)), but only whenever they define a diffeomorphism. This is the case for any open ball of radius $r \leq \pi/2$, as injectivity radius of Grassmannian manifold is $r_g = \pi/2$ (see [4.8](#)).

Nevertheless, it was pointed out in [Lemma 4.10](#) that one can define a logarithmic map outside the injectivity radius (maybe inside the cut-locus as mentioned in [Example 5.2](#)), and thus enable us to make computation on a tangent space. But doing so, there is no way to control what can happen during the procedure.

In the two numerical situations presented in [section 7](#), the interpolation procedure was done, even for cases when Riemannian distance was beyond injectivity radius, as detailed below.

In all cases, recall that for two given points \mathbf{m}_0 and \mathbf{m}_1 in Grassmannian manifold $\mathcal{G}(n; p)$, the Riemannian distance $d(\mathbf{m}_0, \mathbf{m}_1)$ is given by [\(3\)](#).

Issued from the spherical balloon numerical investigation (see [7.2](#)) [Figure B.17](#) produces the Riemannian distance $d(\mathbf{m}_0, \mathbf{m}_i)$ between the reference point \mathbf{m}_0 ($\lambda = 85$) and the points \mathbf{m}_i for $\lambda_i \in \{50; 60; 90\}$, for different modes of the POD (from 1 to 10 modes). The main result here is that distances are below injectivity radius only in the first and the second mode. As it may be interesting, we also propose in [Figure B.18](#) all previous distances normalized with the Grassmannian diameter $\sqrt{p}\pi/2$ (with p being the mode of the

POD). As shown in Figure B.19, where respective distances $d(\mathbf{m}_i, \mathbf{m}_j)$ are given, no any choice would have lead to situation where all points are inside a ball of radius $r \leq r_g$.

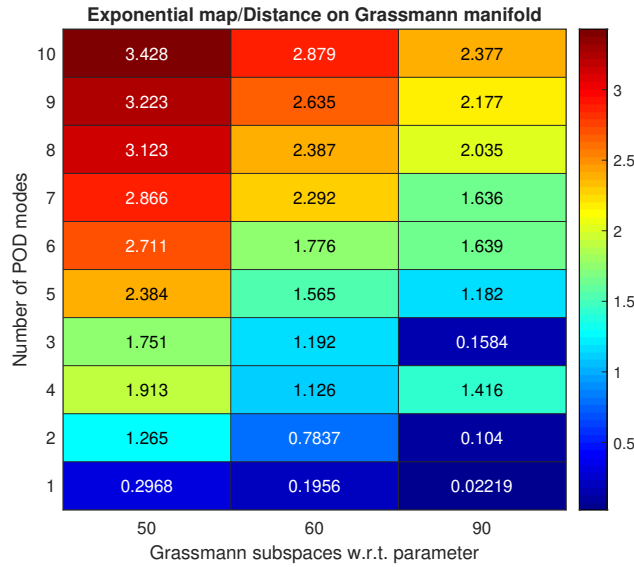


Figure B.17: Distance between subspaces on the Grassmann manifold with respect to the number of POD modes; Reference point: $\mathbf{m}_0(\lambda = 85)$.

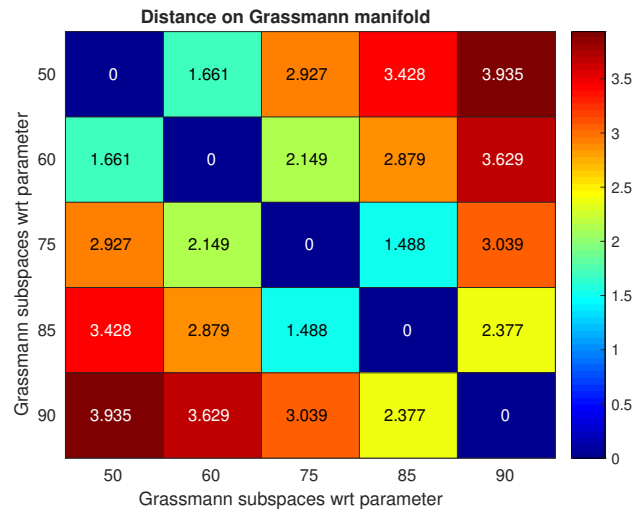


Figure B.19: Distance between subspaces on the Grassmann manifold using the metric $d_r(\mathbf{m}_i, \mathbf{m}_j) = (\sum_{i=1}^p \theta_i^2)^{1/2}$; Number of POD modes $p = 10$.

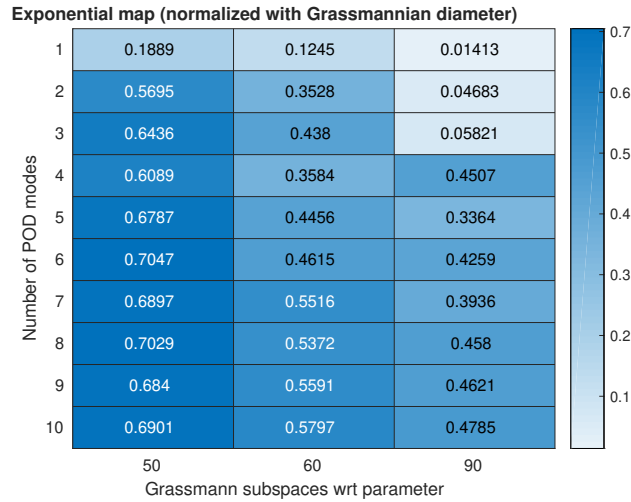


Figure B.18: Distance between subspaces on the Grassmann manifold normalized with the Grassmannian diameter $\sqrt{p}\pi/2$ using the metric $d_r(\mathbf{m}_0, \mathbf{m}_1) = (\sum_{i=1}^p \theta_i^2)^{1/2}$ against the number of POD modes; Reference point: $\mathbf{m}_0(\lambda = 85)$;

References

- [1] Camille Jordan. “Essai sur la géométrie à n dimensions”. In: *Bulletin de la Société mathématique de France* 3 (1875), pp. 103–174.
- [2] Carl Eckart and Gale Young. “The approximation of one matrix by another of lower rank”. In: *Psychometrika* 1.3 (1936), pp. 211–218.
- [3] Kari Karhunen. “Zur spektraltheorie stochastischer prozesse”. In: *Ann. Acad. Sci. Fennicae, AI* 34 (1946).
- [4] Yung-Chow Wong. “Differential geometry of Grassmann manifolds”. In: *Proceedings of the National Academy of Sciences of the United States of America* 57.3 (1967), p. 589.
- [5] Anthony James Merrill Spencer. *Deformations of fibre-reinforced materials*. Oxford, UK ; New York: Clarendon Press, 1972.
- [6] Åke Björck and Gene H Golub. “Numerical methods for computing angles between linear subspaces”. In: *Mathematics of computation* 27.123 (1973), pp. 579–594.
- [7] Gilbert W Stewart. *Introduction to matrix computations*. Elsevier, 1973.

- [8] John M Ball. “Convexity conditions and existence theorems in nonlinear elasticity”. In: *Archive for rational mechanics and Analysis* 63.4 (1976), pp. 337–403.
- [9] M Loève. *Probability theory, Vol. II, Graduate Texts in Mathematics*. Vol. 46. Springer, 1978.
- [10] William M Boothby. *An introduction to differentiable manifolds and Riemannian geometry*. Vol. 120. Academic press, 1986.
- [11] Gene H Golub, Alan Hoffman, and Gilbert W Stewart. “A generalization of the Eckart-Young-Mirsky matrix approximation theorem”. In: *Linear Algebra and its applications* 88 (1987), pp. 317–327.
- [12] MM Mehrabadi and S Nemat-Nasser. “Some basic kinematical relations for finite deformations of continua”. In: *Mechanics of Materials* 6.2 (1987), pp. 127–138.
- [13] Sylvestre Gallot, Dominique Hulin, and Jacques Lafontaine. *Riemannian geometry*. Vol. 2. Springer, 1990.
- [14] JD Humphrey, RK Strumpf, and FCP Yin. “Determination of a constitutive relation for passive myocardium: II. Parameter estimation”. In: *Journal of Biomechanical Engineering* 112.3 (1990), pp. 340–346.
- [15] J Ferrer, MaI García, and F Puerta. “Differentiable families of subspaces”. In: *Linear algebra and its applications* 199 (1994), pp. 229–252.
- [16] R. Everson and L. Sirovich. “Karhunen–Loève procedure for gappy data”. In: *J. Opt. Soc. Am. A* 12.8 (Aug. 1995), pp. 1657–1664. DOI: [10.1364/JOSAA.12.001657](https://doi.org/10.1364/JOSAA.12.001657). URL: <http://josaa.osa.org/abstract.cfm?URI=josaa-12-8-1657>.
- [17] Gene H Golub and CFV Loan. *Matrix Computations, 3rd edn., vol. 1*. 1996.
- [18] Shoshichi Kobayashi and Katsumi Nomizu. *Foundations of differential geometry. Vol. I*. Wiley Classics Library. Reprint of the 1963 original, A Wiley-Interscience Publication. New York: John Wiley & Sons Inc., 1996, pp. xii+329. ISBN: 0-471-15733-3.
- [19] Sergey Emel’yanovich Kozlov. “Geometry of the real Grassmannian manifolds. Parts I, II”. In: *Zapiski Nauchnykh Seminarov POMI* 246 (1997), pp. 84–107.

- [20] Edgard S Almeida and Robert L Spilker. “Finite element formulations for hyperelastic transversely isotropic biphasic soft tissues”. In: *Computer Methods in Applied Mechanics and Engineering* 151.3-4 (1998), pp. 513–538.
- [21] J Bonet and AJ Burton. “A simple orthotropic, transversely isotropic hyperelastic constitutive equation for large strain computations”. In: *Computer methods in applied mechanics and engineering* 162.1-4 (1998), pp. 151–164.
- [22] Alan Edelman, Tomás A Arias, and Steven T Smith. “The geometry of algorithms with orthogonality constraints”. In: *SIAM journal on Matrix Analysis and Applications* 20.2 (1998), pp. 303–353.
- [23] K May-Newman and FCP Yin. “A constitutive law for mitral valve tissue”. In: *Journal of biomechanical engineering* 120.1 (1998), pp. 38–47.
- [24] Mikhail Itskov. “A generalized orthotropic hyperelastic material model with application to incompressible shells”. In: *International Journal for Numerical Methods in Engineering* 50.8 (2001), pp. 1777–1799.
- [25] Gerhard A Holzapfel. “Nonlinear solid mechanics: a continuum approach for engineering science”. In: *Meccanica* 37.4-5 (2002), pp. 489–490.
- [26] IT Jolliffe. *Principal Component Analysis, Series: Springer Series in Statistics, 2nd ed.* NY: Springer, 2002, p. 487.
- [27] Thibault Henri and Jean-Pierre Yvon. “Convergence estimates of POD-Galerkin methods for parabolic problems”. In: *IFIP Conference on System Modeling and Optimization*. Springer. 2003, pp. 295–306.
- [28] P-A Absil, Robert Mahony, and Rodolphe Sepulchre. “Riemannian geometry of Grassmann manifolds with a view on algorithmic computation”. In: *Acta Applicandae Mathematica* 80.2 (2004), pp. 199–220.
- [29] Juan C Simo and Thomas JR Hughes. *Computational inelasticity*. Vol. 7. Springer Science & Business Media, 2006.
- [30] Victorien Prot, Bjorn Skallerud, and GA Holzapfel. “Transversely isotropic membrane shells with application to mitral valve mechanics. Constitutive modelling and finite element implementation”. In: *International journal for numerical methods in engineering* 71.8 (2007), pp. 987–1008.

- [31] P. Astrid et al. “Missing Point Estimation in Models Described by Proper Orthogonal Decomposition”. In: *IEEE Transactions on Automatic Control* 53.10 (2008), pp. 2237–2251.
- [32] David Amsallem et al. “A method for interpolating on manifolds structural dynamics reduced-order models”. In: *International journal for numerical methods in engineering* 80.9 (2009), pp. 1241–1258.
- [33] H Abdi and LJ Williams. “Principal component analysis”. In: *Wiley Interdisciplinary Reviews: Computational Statistics* 2.4 (2010), pp. 433–459.
- [34] Saifon Chaturantabut and Danny C. Sorensen. “Nonlinear Model Reduction via Discrete Empirical Interpolation”. In: *SIAM Journal on Scientific Computing* 32.5 (2010), pp. 2737–2764. DOI: [10.1137/090766498](https://doi.org/10.1137/090766498). eprint: <https://doi.org/10.1137/090766498>. URL: <https://doi.org/10.1137/090766498>.
- [35] Uwe Helmke and John B Moore. *Optimization and dynamical systems*. Springer Science & Business Media, 2012.
- [36] Philip Holmes et al. *Turbulence, coherent structures, dynamical systems and symmetry*. Cambridge university press, 2012.
- [37] S. Niroomandi et al. “Accounting for large deformations in real-time simulations of soft tissues based on reduced-order models”. In: *Computer Methods and Programs in Biomedicine* 105.1 (2012), pp. 1–12. ISSN: 0169-2607. DOI: <https://doi.org/10.1016/j.cmpb.2010.06.012>. URL: <http://www.sciencedirect.com/science/article/pii/S0169260710001653>.
- [38] Kevin Carlberg et al. “The GNAT method for nonlinear model reduction: Effective implementation and application to computational fluid dynamics and turbulent flows”. In: *Journal of Computational Physics* 242 (2013), pp. 623–647. ISSN: 0021-9991. DOI: <https://doi.org/10.1016/j.jcp.2013.02.028>. URL: <http://www.sciencedirect.com/science/article/pii/S0021999113001472>.
- [39] John M Lee. “Smooth manifolds”. In: *Introduction to Smooth Manifolds*. Springer, 2013, pp. 1–31.
- [40] *ABAQUS*. Providence, RI. Standard User’s Manual, Version 6.14. 2014.

- [41] Elías Cueto and Francisco Chinesta. “Real time simulation for computational surgery: a review”. In: *Advanced Modeling and Simulation in Engineering Sciences* 1.11 (2014). DOI: [10.1186/2213-7467-1-11](https://doi.org/10.1186/2213-7467-1-11). URL: <https://hal.archives-ouvertes.fr/hal-01590981>.
- [42] Peter Benner, Serkan Gugercin, and Karen Willcox. “A Survey of Projection-Based Model Reduction Methods for Parametric Dynamical Systems.” In: *SIAM Review* 57.4 (2015), pp. 483–531. URL: <http://dblp.uni-trier.de/db/journals/siamrev/siamrev57.html#BennerGW15>.
- [43] Annika Radermacher and Stefanie Reese. “POD-based model reduction with empirical interpolation applied to nonlinear elasticity”. In: *International Journal for Numerical Methods in Engineering* 107.6 (2016), pp. 477–495. DOI: [10.1002/nme.5177](https://doi.org/10.1002/nme.5177). eprint: <https://onlinelibrary.wiley.com/doi/pdf/10.1002/nme.5177>. URL: <https://onlinelibrary.wiley.com/doi/abs/10.1002/nme.5177>.
- [44] John M Lee. *Introduction to Riemannian manifolds*. Vol. 176. Springer, 2018.
- [45] Rolando Mosquera Meza. “Interpolation sur les variétés grassmanniennes et applications à la réduction de modèles en mécanique”. PhD thesis. La Rochelle, 2018.
- [46] Rolando Mosquera et al. “POD basis interpolation via Inverse Distance Weighting on Grassmann manifolds”. In: *Discrete & Continuous Dynamical Systems-S* 12.6 (2018), p. 1743.
- [47] M Oulghelou and C Allery. “Non intrusive method for parametric model order reduction using a bi-calibrated interpolation on the Grassmann manifold”. In: *arXiv preprint arXiv:1901.03177* (2018).
- [48] Rolando Mosquera et al. “Generalization of the Neville-Aitken Interpolation Algorithm on Grassmann Manifolds: Applications to Reduced Order Model”. In: *arXiv preprint arXiv:1907.02831* (2019).
- [49] Mariano Vázquez et al. *Advanced HPC-based Computational Modeling in Biomechanics and Systems Biology*. Lausanne: Frontiers Media, 2019.
- [50] Ralf Zimmermann. *Manifold interpolation and model reduction*. 2019. arXiv: [1902.06502](https://arxiv.org/abs/1902.06502) [[math.NA](https://arxiv.org/abs/1902.06502)].

- [51] Charbel Farhat and David Amsallem. “Recent Advances in Reduced-Order Modeling and Application to Nonlinear Computational Aeroelasticity”. In: *46th AIAA Aerospace Sciences Meeting and Exhibit*. DOI: [10.2514/6.2008-562](https://doi.org/10.2514/6.2008-562). eprint: <https://arc.aiaa.org/doi/pdf/10.2514/6.2008-562>. URL: <https://arc.aiaa.org/doi/abs/10.2514/6.2008-562>.